Study of Sodium Colour Centres in Diamond for Quantum Technology Applications

Guilherme Jesus da Cunha Santos
Master in Engineering Physics
Department of Physics and Astronomy
Faculty of Sciences and Faculty of Engineering of the
University of Porto
2024/2025

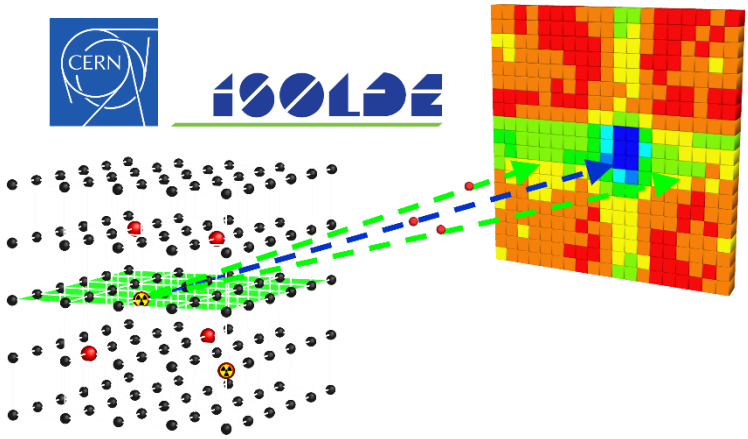

Study of Sodium Colour Centres in Diamond for Quantum Technology Applications

Guilherme Jesus da Cunha Santos

Dissertation carried out as part of the Master in Engineering Physics

Department of Physics and Astronomy

2024/2025

Supervisor

João Pedro Esteves de Araújo, Associate Professor with Habilitation, Faculty of Sciences of the University of Porto

Co-supervisor

Ulrich Wahl, Principal Investigator with Habilitation, Department of Engineering and Nuclear Sciences, Instituto Superior Técnico, University of Lisbon

IFIMUP

Institute of Physics for Advanced Materials, Nanotechnology, and Photonics

University of Porto

C²TN

CENTRO DE CIÊNCIAS E TECNOLOGIAS NUCLEARES

Acknowledgements

I would like to express my gratitude to my supervisor, Dr João Pedro Araújo, and my co-supervisor, Dr Ulrich Wahl, for their guidance and support throughout this thesis, for their company during breaks and meals, and for their assistance in the writing and review of this document.

I am also grateful to Dr João Guilherme Correia for his guidance, having taught me much of the laboratory work conducted at ISOLDE/CERN, and to all the other collaborators who worked with me and allowed me to carry out research at ISOLDE/CERN, including Dr Lino Pereira, Dr Ângelo Costa, and the PhD students Kirill Danilov, Brecht Biesmans, and Afonso Lamelas.

I would like to acknowledge the project number 2024.00223.CERN, funded by measure RE-C06-i06.m02 - “Strengthening the funding of International Partnerships in Science, Technology and Innovation” of the Recovery and Resilience Plan (PRR), under the agreement between the Recovery Portugal Mission Structure (EMRP) and the Foundation for Science and Technology (FCT), as intermediate beneficiary. I would also like to thank the unit project of IFIMUP and LaPMET from the Faculty of Sciences of the University of Porto.

I am grateful to my friends, who supported me in my academic work and kept me motivated throughout this journey. I would also like to thank all my professors, whose guidance contributed significantly to my academic and personal growth.

I am sincerely thankful to my cousin Bruna Fonseca and Soufian Lachhab for hosting me at their home, and to all their family for the wonderful meals, conversations, and trips.

Finally, I would like to express my sincere gratitude to my family, particularly my parents, for their constant support and kindness during the time I was far from home. I am also deeply grateful to my girlfriend, Ângela Lopes, for her encouragement, unwavering support, and companionship throughout my entire academic journey, which helped bring this chapter to a successful and memorable conclusion.

This thesis is dedicated to the memory of my grandfather, José Gomes Cruz, whose guidance and example continue to inspire me.

Resumo

Os centros de cor em diamantes representam uma das áreas de investigação mais ativamente estudadas no campo das tecnologias quânticas. Neste trabalho, estudou-se um centro de cor específico baseado em sódio (Na), selecionado devido às previsões teóricas promissoras, que sugerem o seu potencial para diversas aplicações quânticas, apesar da atual falta de estudos experimentais. Para explorar este centro, realizaram-se duas experiências complementares no ISOLDE/CERN. Primeiro, realizou-se a técnica de *Emission Channeling* (EC) para determinar os locais mais prováveis para o sódio, ^{24}Na radioativo, ocupar na rede cristalina de um diamante. Em seguida, utilizou-se um sistema de fotoluminescência (PL) para obter o espectro de emissão de uma amostra semelhante implantada com ^{23}Na estável. As medições de EC revelaram que o sódio provavelmente adopta uma combinação de configurações substitucionais (S) e de *bond-centre* (BC), maximizada após uma temperatura de recozimento de 600°C, exibindo aproximadamente 51% de *split-vacancy* NaV (a fração mais alta observada) e 17% de Na substitucional (que aumenta lentamente e quase linearmente com a temperatura de recozimento). No entanto, a temperaturas de recozimento mais elevadas, a configuração BC diminui rapidamente, e a fração combinada destas duas configurações também decresce, sugerindo o surgimento de uma outra configuração ainda não identificada. Na experiência de PL, não se observou um sinal ótico direto atribuível ao sódio, mas apresentou-se a caracterização óptica das amostras de diamante monocristalino fabricadas pela Element Six e implantadas com sódio estável a diferentes temperaturas de recozimento. Verificou-se que o centro 3H está consistentemente presente em quase todas as amostras após a implantação e o recozimento, com o seu pico de zero fonões (ZPL) localizado em torno de 503 nm.

Palavras-chave: Centros de cor em diamantes, ISOLDE/CERN, Tecnologias Quânticas, Fotoluminescência, Emission Channeling, Impurezas de Sódio

Abstract

Colour centres in diamonds represent one of the most actively researched areas in the field of quantum technologies. In this work, we investigate a specific colour centre based on sodium (Na), selected due to promising theoretical predictions suggesting its potential for various quantum applications, despite the current lack of experimental studies. To explore this centre, we conducted two complementary experiments at ISOLDE/CERN. First, we employed the electron emission channeling (EC) technique to determine the most probable lattice sites occupied by sodium in a single-crystal lattice of a diamond implanted with radioactive ^{24}Na. We then used a photoluminescence (PL) set-up to obtain the emission spectrum of a similar sample implanted with stable ^{23}Na. EC measurements revealed that sodium likely adopts a combination of substitutional (S) and bond-centre (BC) sites, maximised after an annealing temperature of 600°C, exhibiting approximately 51% NaV split-vacancy (the highest fraction observed) and 17% substitutional Na (which increases slowly and almost linearly with annealing temperature). However, at higher annealing temperatures, the BC configuration decreases rapidly, and the combined fraction of these two sites also drops, suggesting the emergence of another, yet unidentified, configuration. In the PL experiments, we did not observe a direct optical signal attributable to sodium, but we present the optical characterisation of single-crystal diamond samples fabricated by Element Six and implanted with stable sodium at different annealing temperatures. We found the 3H centre consistently present across nearly all samples following implantation and annealing, with its zero-phonon line (ZPL) located around 503 nm.

Keywords: Colour centres in Diamonds, ISOLDE/CERN, Quantum Technologies, Photoluminescence, Emission Channeling, Sodium Impurities

Table of Contents

List of Figures

Glossary

APT	Aperture
AVG	Average
BC	Bond-Centre
CCD	Charge-Coupled Device
CVD	Chemical Vapour Deposition
CW	Central Wavelenght
DFT	Density Functional Theory
DW	Debye-Waller factor
EC	Emission Channeling
EL	Electronic grade
ET	Exposure Time
FCA	Franck-Condon Absorption
FCE	Franck-Condon Emission
FND	Fluorescent NanoDiamond
FWHM	Full Width at Half Maximum
GHM	General High Mass
GLM	General Low Mass
GPS	General Purpose Separator
HPHT	High Pressure High Temperature
HRS	High Resolution Separator
MPCVD	Microwave Plasma-enhanced Chemical Vapour Deposition
Na_S	Substitutional Sodium
NaV	Sodium-Vacancy
NV	Nitrogen-Vacancy
PL	Photoluminescence
PSB	Phonon Sideband
PSD	Position-Sensitive Detector
RIB	Radioactive Ion Beam
RMS	Root-Mean-Square
rPL	Radiotracer Photoluminescence
RT	Room Temperature

S	Substitutional
SC	Single-Crystal
STK	Stack
VM	Vibrational Mode
ZPL	Zero-Phonon Line

1. Theoretical and Conceptual Background

1.1. Colour centres in diamonds

1.1.1 Diamond

Diamond is commonly known as the hardest natural material [1] and is extensively used as an expensive gemstone, with multiple colours [2].

Carbon is an element in the second period and in group IV, with an atomic number of 6 and a mass number of 12. Its ground-state electronic configuration is $1s^2\ 2s^2\ 2p^2$, presenting four outer electrons (valence electrons). In the diamond crystal, the carbons share one electron with each one of the four neighbours (in sp^3 hybrid orbitals), resulting in a tetrahedral arrangement. This type of bonding is a simple covalent bond, which is a very strong bond between carbon atoms [3].

The diamond bandgap is 5.47 eV (at 300 K), which is considered a very large bandgap, making it an electrical insulator. In fact, at room temperature, almost no electrons are thermally excited to the conduction band. On the other hand, diamond has the highest room-temperature thermal conductivity of any conventional solid. In this case, the heat is transferred via phonons (atomic vibrations) in contrast to metals, where the electrons carry the heat [3].

In a pure diamond (defect-free), light can be absorbed with two mechanisms:

- Via ultraviolet radiation, if the energy of the photons is greater than the bandgap energy ($\lambda <$223 nm), generating electron-hole pairs, giving rise to the absorption edge;

- Via infrared radiation, the absorbed light generates phonons, causing the carbon atoms to vibrate ($2.5 < \lambda < 6.5\ \mu$m), giving rise to the phonon absorption region.

This means that defect-free diamonds are **transparent** to the visible region ($0.4 < \lambda < 0.7\ \mu$m) and should not show any type of colour; they are colourless (Fig.1.1). Most diamonds found in nature have colour, so light must be absorbed in the visible region. This absorption arises from the presence of defects in the diamond.

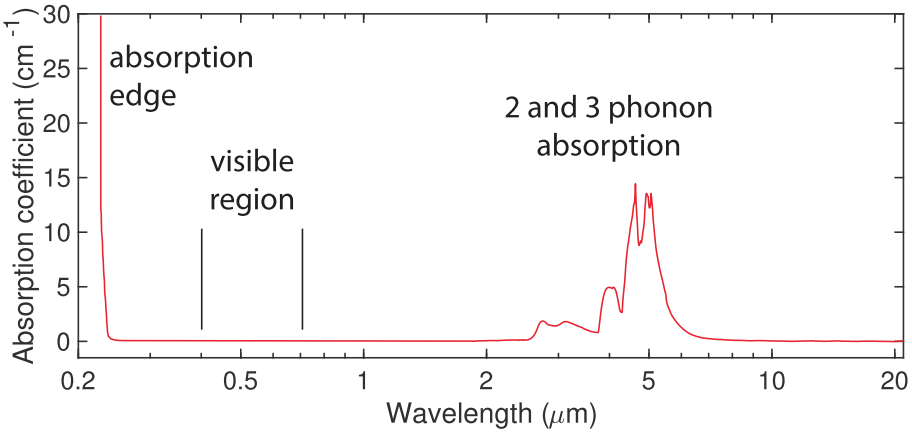

Figure 1.1: Diamond electromagnetic absorption spectrum [2].

1.1.2 Diamond Crystal Structure

The crystal structure of diamond is one of the most studied crystal structures. It can be described as a face-centred cubic (FCC) lattice with a basis of two carbon atoms at $(0,0,0)$ and $(\frac{1}{4},\frac{1}{4},\frac{1}{4})$, which is equivalent to two interpenetrating FCC lattices offset along a body diagonal by one-quarter of its length. The conventional cubic unit cell has a lattice parameter $a_0 = 3.57$ Å, and the nearest-neighbour carbon bond length follows as $d = \frac{\sqrt{3}}{4}a_0 = 1.54$ Å.

If we imagine that each atom is a sphere, we can say that the conventional cell contains the equivalent of eight whole carbon atoms. The theoretically calculated mass density for diamond is then, $\rho_m = 8/a_0^3 \times m_{\text{one carbon atom}} = 3.516$ g/cm^3.

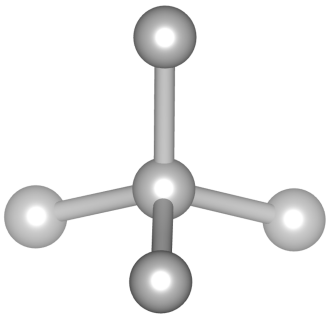

Figure 1.2: Tetrahedral configuration of diamond.

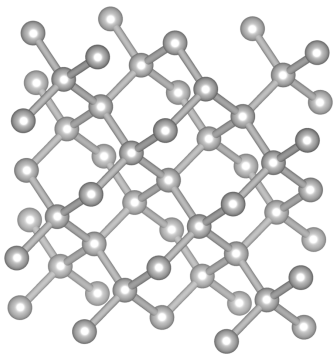

Figure 1.3: Diamond lattice.

1.1.3 Defects in Diamond

As already mentioned, most diamonds found in nature present a colour, which is due to the impurities present in the solid. The most common impurity found in natural diamonds

is nitrogen, which is found in more than 98% of natural diamonds. The second most common impurity is boron [4].

The most common method of classifying diamonds is based on the presence or absence of certain impurities, such as nitrogen and boron, which can be detected by infrared (IR) spectroscopy. Type I diamonds contain nitrogen, while type II diamonds do not. Inside type II, if boron is not detectable, it is type IIa; if it is detectable, it is type IIb. See more about diamond classification in [2].

The common name that the science community uses to refer to optically active defects in diamond is colour centres. Colour because these defects can absorb and emit light in the visible region (defect-free diamond does not), and centre refers to a localised imperfection in the crystal lattice, such as vacancies, impurity atoms, complexes, etc, that introduce additional localised electronic levels into the electronic band structure of the diamond, leading to distinct optical transitions.

We can visualise the high-symmetric lattice sites in a diamond in the following figure:

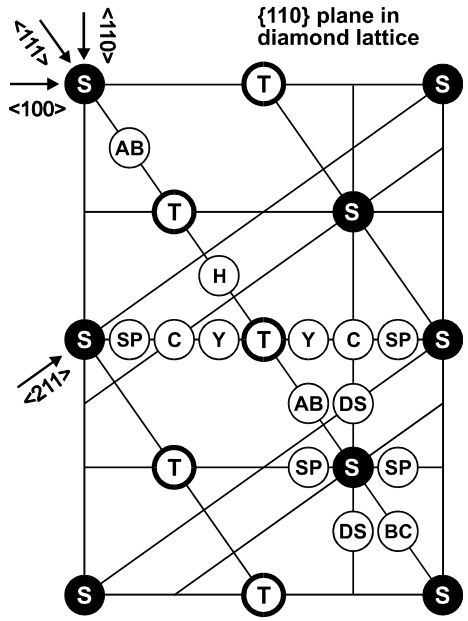

Figure 1.4: High-symmetric sites in {110} plane in diamond lattice [5].

The figure shows part of the {110} planes of the diamond lattice. The letters in the figure correspond to specific high-symmetry lattice sites: substitutional (S), interstitial tetrahedral (T), bond-centre (BC), hexagonal (H), anti-bonding (Q or AB), split $\langle 100 \rangle$ (SP), split $\langle 110 \rangle$ (DS), Ytterbium (Y), and “C” sites. The most commonly occupied sites are S, BC, and T, depending on the impurity’s atomic size and chemical properties.

1.1.4 Synthetic Diamonds

The **High Pressure High Temperature** (**HPHT**) method used to be the most common way to grow diamonds. It consists of inserting some carbon source with a metal catalyst in a reactor chamber capable of achieving enormous pressures (6 GPa) and temperatures (1600°C). With a seed crystal in the chamber, it is possible to grow diamond single crystals [6].

Nowadays, the most common technique used is **Chemical Vapour Deposition** (**CVD**), and to achieve high-purity single crystals, the most widely adopted method is **Microwave Plasma-enhanced Chemical Vapour Deposition** (**MPCVD**). Diamond is synthesised from a hydrogen-rich H_2/CH_4 plasma, where CH_3 radicals act as key precursors, and atomic hydrogen stabilises the diamond phase by etching sp^2 carbon [7].

The company Element Six fabricated our MPCVD single-crystal (**SC**) diamonds with the following characteristics: crystallography - single sector {100} on the top faces; edge orientation - $\langle 100 \rangle$ edges; face orientation - {100} faces; dimensions - 3.0 $\times$ 3.0 mm^2 surface area and 0.25 mm thickness; with [N] < 1 ppm [8, 9]. Our electronic grade MPCVD single-crystal (EL SC, or **EL** to distinguish) diamonds have the following characteristics: crystallography - single sector {100} on the top faces; edge orientation - $\langle 110 \rangle$ edges; face orientation - {100} faces; dimensions - 2.0 $\times$ 2.0 mm^2 surface area and 0.50 mm thickness; with [N_s^0] < 5 ppb [10].

1.1.5 Annealing

Annealing is a thermal treatment in which a material is heated to a specific temperature, held at that temperature (soaking), and then cooled down in a controlled way. This process is widely used in materials science and engineering to relieve internal stresses, and **repair damage in the crystal lattice**. It can also be used to modify electrical or optical properties, especially in semiconductors, metals, or, in the context of this thesis, in the study of defects in diamond. Through annealing, dopants can be activated and impurities may migrate to energetically favourable lattice sites, allowing the system to reach a lower energy state [11].

In semiconductor and ion implantation experiments, such as with diamond, annealing is essential for repairing the lattice from implantation damage caused by high-energy implanted ions and for stabilising dopants or colour centres. By promoting atomic diffusion, annealing may enable implanted atoms to occupy energetically favourable sites, which is

crucial for obtaining reliable and meaningful experimental results. A further role of annealing may be the stabilisation of the charge state of certain defects in different materials, allowing them to exhibit optically accessible transitions.

1.1.6 Photoluminescence

Luminescence is the general physical phenomenon where a material emits light after being excited by an external energy source. If that energy source is light, the process is known as photoluminescence (PL). In this case, the material absorbs photons of a certain energy, which excites electrons to higher energy states; these electrons then return to lower energy states via the emission of light, generally of the same or lower energy. If energy is lost through non-radiative processes, typically via phonon interactions - a phonon being a quantum of vibrational energy in a crystal lattice, essentially a particle-like representation of collective atomic vibrations - the emitted light has lower energy [2, 6].

Luminescence can occur via two processes: **fluorescence** or **phosphorescence**. The main difference between them lies in the timescale on which they occur: fluorescence is much faster, whereas phosphorescence occurs over a longer period and is more noticeable, as it persists even after the excitation light is turned off.

In Fig.1.5, we can see these processes illustrated. The figure shows absorbance; internal conversion, where a vibrational state of an electronically excited state couples to a vibrational state of a lower electronic state; and intersystem crossing, which is a transition to a state with a different spin multiplicity. One of the most important processes is **vibrational relaxation**, which involves the dissipation of energy from the excited species to its surroundings. This process plays a significant role in the study of colour centres in diamond. The figure also shows the approximate number of interactions per second for each process, with absorbance being the fastest and phosphorescence the slowest [12].

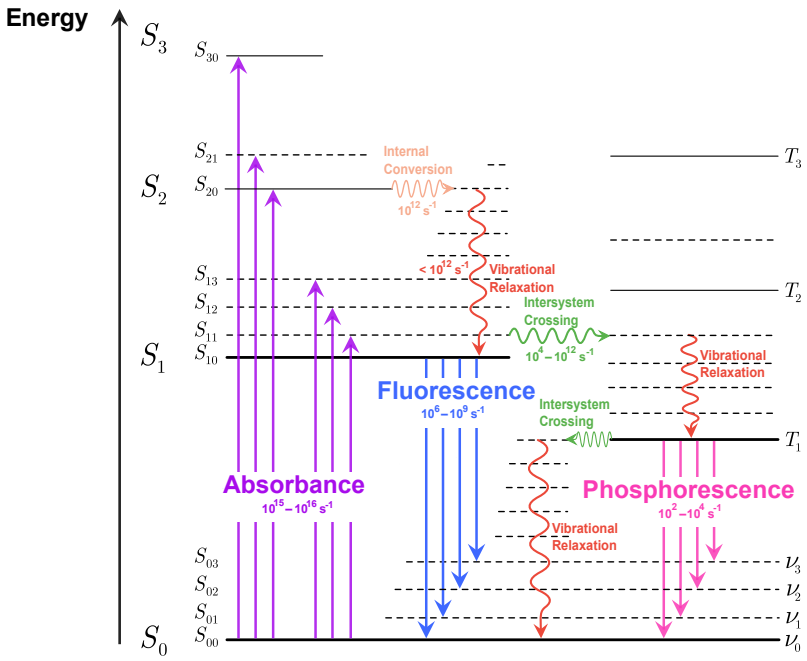

Figure 1.5: Luminescence: *S* denotes singlet electronic states, *T* denotes triplet electronic states, and ν represents vibrational energy levels within each electronic state. Adapted from [12].

In a common PL spectroscopy experiment, when the incoming photons have an energy equal to or larger than the material's bandgap, electron-hole pairs are created. If that energy is greater than the material's bandgap energy, the electrons will go to an excited state, and they will quickly thermalise to the bottom of the conduction band (via a non-radiative process). The electron-hole pairs eventually will recombine, emitting photons with approximately the energy of the bandgap [3].

In our case, we do not excite with above-bandgap photons. Instead, **excitation** occurs directly through the defect states, without generating electron-hole pairs. The process is quasi-resonant, where photons with slightly higher energy than the Zero-Phonon Line (ZPL) excite directly the defect via the Phonon Sideband (PSB). The excess energy is transferred to phonons. The subsequent **emission** occurs close to the ZPL energy, and may involve phonon-assisted emission or occur directly at the ZPL.

The electron-phonon coupling can be described with the **vibronic coordinate diagram** in Fig.1.6. Each parabola represents an electronic state; the one on the left, with smaller energy, is the ground state, centred in Q_g, and the other, with greater energy, is the first excited state, centred in Q_e. The blue lines represent the different vibrational modes (VMs) in each electronic state, with different energy spacings [3].

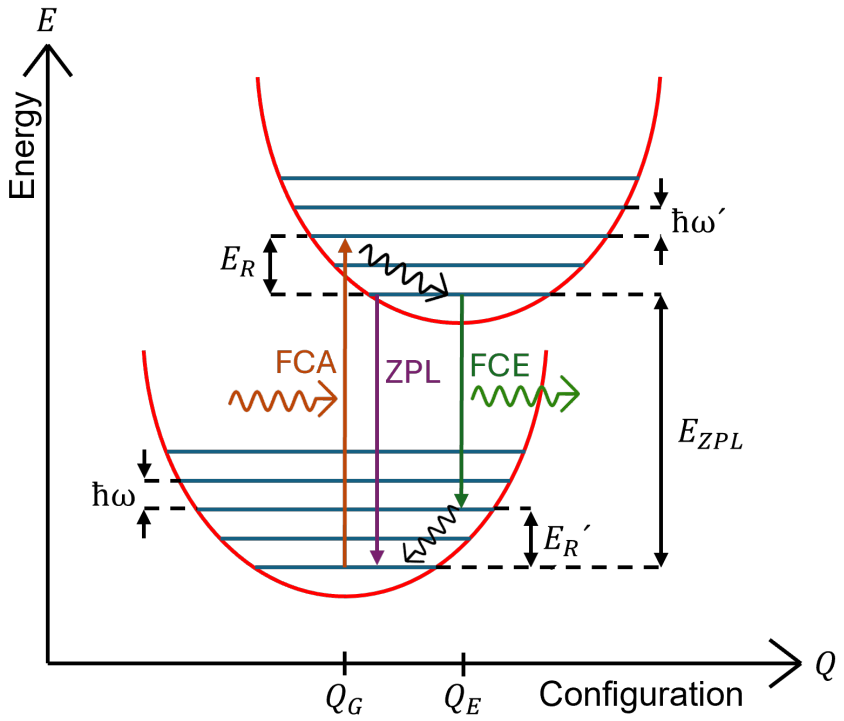

Figure 1.6: Vibronic coordinate diagram.

The **Franck–Condon principle** states that the probability of a transition between two electronic states is proportional to the overlap between their vibrational wave functions (i.e., phonon states). The most likely transition between the ground-state and the excited-state is the vertical transition, known as **Franck-Condon absorption** (**FCA**) [13].

Thereafter, the system will thermalise into the lowest-energy VM of the excited state, and then the centre may relax to the ground state, emitting a photon with energy, hf_0, and no phonons (pure electronic transition). In the PL spectrum, the corresponding line is the zero-phonon line (ZPL), which corresponds to the photon with higher energy.

The **Franck-Condon emission** (**FCE**) occurs as the system undergoes a vertical downward transition to an excited VM of the ground-state configuration. Subsequently, the system relaxes further by emitting multiple phonons with energy $\hbar w$, eventually reaching the lowest-energy VM of the ground state. These emissions have lower energies than the ZPL transition, resulting in several peaks, known as vibronic sidebands [3].

In **quantum applications**, it is important to have emitters with a well-defined frequency, so we want to maximise the intensity of ZPL and minimise the intensity of vibronic sidebands. The centre most used is the nitrogen-vacancy (NV) centre, but this centre has a problem, which is that its ZPL intensity is low, i.e. a low Debye-Waller factor (cf. definition below,

only around 3–4% at RT [14–16]), even though it is very sharp, so we want to find new materials with a high ZPL intensity.

One of the most important characteristics of colour centres is their **charge state**, which can be neutral, positively charged, or negatively charged. In fact, different charge states correspond to completely different local atomic systems with distinct electronic configurations and symmetries. This determines whether a given defect is optically active and whether a zero-phonon line is present at all. Annealing can play a key role in modifying and stabilising the charge state of a defect, thereby enabling optically accessible transitions.

1.1.7 Debye-Waller Factor

The Debye-Waller factor (DW) is a good experimental parameter to describe the coupling between the electrons and the phonons. It is defined as:

$$DW = \frac{I_{ZPL}}{I_{\text{total}}} = \frac{I_{ZPL}}{I_{ZPL} + I_{PSB}} \tag{1.1}$$

where I_{ZPL} and I_{PSB} are the intensities of the zero-phonon line (ZPL) and the phonon sideband (PSB), respectively. This ratio tells us the amount of intensity present in the zero-phonon line, compared to the total intensity of the emission spectrum. As noted earlier, in quantum applications, we want a narrow ZPL and low phonon sidebands, corresponding to a Debye-Waller factor near one, which means we are in the presence of weak coupling. For strong coupling between electrons and phonons, the factor is close to zero, which means that our ZPL intensity is much smaller than the intensity of the phonon sideband. The Debye-Waller factor is a good parameter to compare the results of different centres [17].

1.1.8 Radiotracer Photoluminescence - rPL

Radiotracer photoluminescence (rPL) enhances the conclusions that can be drawn from standard PL by introducing radioactive isotopes, allowing for **chemical identification** through time-dependent changes in PL intensity. As radioactive isotopes decay into daughter elements, the corresponding PL lines grow or diminish according to the half-lives of each isotope. This method overcomes the chemical blindness of conventional PL, which typically cannot directly identify the chemical nature of defects, especially for heavier elements where isotopic shifts are too small to detect [18–20].

1.1.9 Raman Scattering

Raman scattering, in contrast to Rayleigh scattering, involves a change in the energy of the scattered photons. While Rayleigh scattering is elastic (the energy of the incident and scattered photons is conserved), Raman scattering is inelastic. In this process, the photon either loses or gains energy through interaction with a vibrational mode (phonon) in the crystal lattice [2].

In **Stokes scattering**, the incident photon loses energy, creating a phonon in the lattice. In **anti-Stokes scattering**, the photon gains energy by absorbing an existing phonon.

The energy of a phonon is typically represented by $\hbar\Omega$. The energies of the Stokes and anti-Stokes scattered photons can be written as:

$$h\nu_s = h\nu - \hbar\Omega \tag{1.2}$$

$$h\nu_{as} = h\nu + \hbar\Omega \tag{1.3}$$

Where h is Planck's constant, ν is the frequency of the incident photon, ν_s is the frequency of the emitted photon in the Stokes scattering and ν_{as} is the frequency of the emitted photon in the anti-Stokes scattering.

At room temperature and below, anti-Stokes scattering is much weaker than Stokes scattering because the thermal population of phonons is low. As a result, the probability of a photon interacting with and absorbing a phonon is much smaller than that of creating one.

The Raman shift is material-dependent. In diamond, the characteristic first-order Raman peak appears as a sharp and intense feature at a shift of 1333 cm^{-1} relative to the energy of the incident light. A weaker and broader second-order peak is typically observed at a shift of 2667 cm^{-1}, corresponding to two-phonon scattering processes [2].

To estimate the wavelength of the **Stokes-shifted** light, given a laser of wavelength λ_0, the Raman-shifted wavelength λ_s can be approximately calculated using the relation:

$$\frac{1}{\lambda_s} = \frac{1}{\lambda_0} - \Delta\tilde{\nu} \tag{1.4}$$

where λ_0 is the laser wavelength (in cm), λ_s is the scattered wavelength (in cm), and $\Delta\tilde{\nu}$ is the Raman shift expressed in wavenumbers (cm^{-1}).

If $\Delta\tilde{\nu} = 1333$ cm^{-1} for diamond, we are referring to the first-order Raman shift.

1.1.10 Sodium (Na) Centres

Sodium (Na) centres were selected for this study because theoretical predictions indicate that this centre has potential for various quantum applications. From the experimental side, the knowledge of Na in diamond is scarce.

One of the latest works on the Na centres was carried out by Joel Davidsson *et al* [21], who used the ADAQ (Automatic Defect Analysis and Qualification) high-throughput computational database to investigate defects with high spin states. In that study, they investigated a great number of defects, but the ones that stand out more were the Sodium Substitutional (Na_s) and Sodium-Vacancy (NaV), as shown in Fig.1.7. On these defects, they used higher-order methods, such as HSE DFT (Heyd–Scuseria–Ernzerhof hybrid Density Functional Theory) calculation, to confirm their properties.

Density Functional Theory (**DFT**) is a quantum mechanical method used in simulations that models many-electron systems using the electron density rather than the full wavefunction, using approximations for the exchange-correlation energy. Researchers commonly use it to predict structural, electronic, and optical properties in physics, chemistry, and materials science. HSE DFT (Heyd-Scuseria-Ernzerhof) is a type of DFT that improves accuracy by mixing DFT with a portion of exact exchange from Hartree-Fock, especially effective for bandgap predictions in solids, like the colour centres we are studying [22].

In Lombardi's article [23], they studied sodium in diamond with *ab initio* density functional theory (DFT), and they found that the Na substitutional site is more stable than the tetrahedral interstitial site (T), with the formation energy of substitutional Na 2.87 eV lower than the interstitial site.

Na substitutional is a promising defect for quantum applications, due to the multiple spin states for different charge states, but it hasn't been studied much further yet. Its charge depends on the doping of the host material, and each charge state (2-, 1-, 0, 1+) has different spin states. Besides the charge 1+, all the other present ZPL transitions with similar values of ZPL [21].

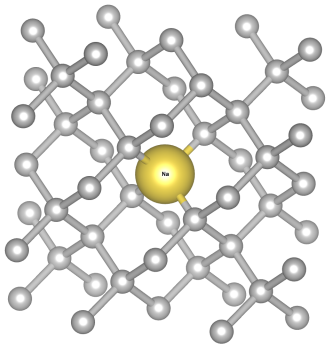

(a) Substitutional Na.

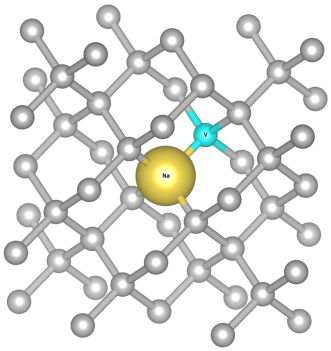

(b) NaV / “full-vacancy” configuration: substitutional Na with a neighbouring vacancy. This configuration of NaV is theoretically predicted to be unstable [21].

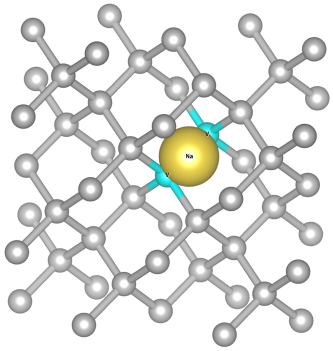

(c) NaV / “split-vacancy” configuration: can be pictured as Na on the bond-centre (BC) side inside a double vacancy.

Figure 1.7: Na possible configurations.

The most interesting charge states are the -1 and 0 (neutral), because they are predicted to have a bright ZPL in the near-infrared regions and a high Debye-Waller factor around 40-77% [21], with spin 1 and 3/2, respectively. Na_s centres are predicted to exhibit properties that make them highly promising for biological sensing applications, outperforming NV centres due to their bright near-infrared ZPL, potentially lower spectral diffusion, and significantly higher Debye-Waller factor.

In diamond, it is an open question whether sodium implantation leads to the formation of substitutional Na_s centres, NaV centres with a split- or full-vacancy configuration, or both. This thesis investigates the nature and configuration of these sodium-related defects. The ADAQ database reports that NaV has a slightly lower formation energy than Na_s, so it should be more stable and more likely to be formed, and it exhibits the split-vacancy configuration [21]. Alkali metals and alkaline earths have similar chemical properties, and since Na is a neighbour of Mg in the periodic table, the amount of lattice defects created during ion implantation is also comparable. One might therefore expect both elements to exhibit a similar lattice site distribution following ion implantation [24].

In the negative charge state, the NaV centre is predicted by the database to have spin 2, with an allowed ZPL transition at 2.548 eV, which corresponds to a wavelength of 487 nm. These energy and wavelength values are comparable to the ZPL transition of the MgV centre, reported as 2.224 eV (554 nm) [21].

The database also lists a ZPL at 1.592 eV (779 nm) or 1.49 eV (832 nm) for the Na_s centre, which we will be looking for in both configurations during our PL measurements [21].

1.1.11 Quantum Technology Applications

Diamond colour centres can be treated as spin systems whose quantum states can be manipulated and controlled for technological applications. This is due to the presence of an unpaired electron, whose spin state can be initialised, manipulated, and optically read out. The resulting spin state coherence is a key feature that makes these centres particularly valuable in quantum technologies. The **nitrogen-vacancy** (**NV**) centre is the most extensively studied among them, with almost 50 years of NV research [25]. As we can see in Fig.1.8, the nitrogen atom in the NV centre is much smaller compared to the sodium atom in the previous configurations. Because of this smaller size, it is easier for the nitrogen atom to fit into the lattice, which is why many nitrogen-related centres exist.

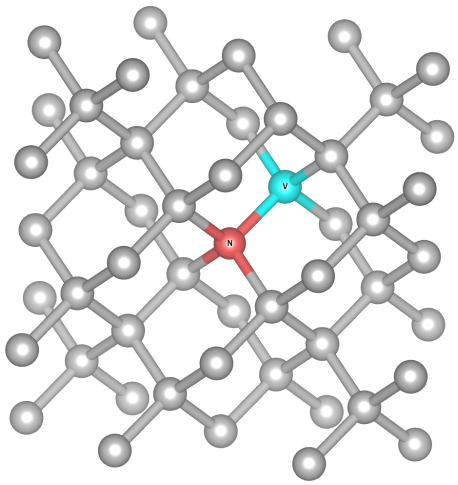

Figure 1.8: NV / “full-vacancy” configuration: substitutional N with a neighbouring vacancy.

Nitrogen-vacancy (NV) centres in diamond have garnered significant attention in recent years due to their unique combination of optical and spin properties, which remain stable at room temperature. These defect centres possess long spin coherence times, which can be optically initialised and read out, and can interact sensitively with external fields [25].

These characteristics make NV centres versatile for a wide range of cutting-edge technologies, such as:

Quantum sensing due to the coupling of the centre with the environment; it can couple with a magnetic field (high precision magnetometer), an electric field, strain, and temperature. This results in relative shifts in the energies of the spin sublevels and changes in the transition rates between them, which can be measured with optical readout, optical spin polarisations, and coherent microwave control [26, 27].

In the **health and biomedical fields**, we can find that Fluorescent NanoDiamonds (FNDs) offer major advantages over traditional biomarkers like Green Fluorescent Protein and quantum dots due to their brightness, photostability, and biocompatibility. They can be functionalised with biomolecules or DNA for targeted applications. Nanodiamonds as small as 7–19 nm have been used successfully in cellular imaging and tracking, with efforts ongoing to develop even smaller, brighter, and more stable particles. Real-time imaging, drug delivery, and targeted bio-labelling have all been demonstrated using FNDs. However, challenges remain in producing high-quality colour centres in small nanodiamonds and in preventing agglomeration [28].

In **quantum computing**, the NV centres in diamond are promising building blocks for quantum technologies due to their long spin coherence times, at room temperature, and their optical addressability. They enable high-fidelity control and readout of both electron and nuclear spins, forming the basis for quantum bits and quantum registers. Their solid-state nature allows integration with photonic and electronic devices, though challenges remain in fabrication precision and photon collection efficiency [29].

Single-photon emitters are essential for quantum technologies such as quantum communication, quantum computing, and quantum cryptography, where individual photons are used to carry and process quantum information. The nitrogen-vacancy centre has important limitations as a single-photon source. Most notably, its ZPL contributes only a small fraction (3-4%) of the total emission, with the majority emitted into broad phonon sidebands. This results in spectrally broad and less coherent photons, making the NV centre less suitable for applications requiring high photon indistinguishability and narrow emission lines. To overcome these limitations, various studies have focused on group-IV colour centres in diamond, such as SiV, SnV, GeV, and PbV. These defects exhibit narrower ZPLs, higher emission rates into the ZPL, reduced phonon coupling, and greater

spectral stability. Such features make them highly promising for the development of scalable, stable single-photon sources, well-suited for integration into nanophotonic circuits and quantum networks [30–32].

1.2. Electron Emission Channeling

The Emission Channeling Technique is a powerful method for determining the lattice site occupancy of radioactive isotopes in single crystals. It is based on the fact that charged particles that are isotropically emitted during nuclear decay, such as beta particles, conversion electrons, positrons, or alpha particles, may experience a series of correlated scattering events with the atomic nuclei within crystallographic axes and planes inside a single crystal, which results in highly anisotropic emission of these particles from the surface of the monocrystalline. In the case of beta decay, which involves the emission of electrons, the technique is specifically referred to as Electron Emission Channeling [33–36].

1.2.1 Beta (β) Decay

Beta (β) decay is a nuclear process from the weak-interaction decay in which a neutron is transformed into a proton (or vice versa), accompanied by the emission of an electron or positron and a neutrino. Beta decay exists in three different variants, as we can see below. In all cases, the number of nucleons A (mass number) remains the same, while the nuclear charge Z (atomic number) will increase or decrease by one unit (± 1) [5, 37]:

$$\mathrm{n} \rightarrow \mathrm{p} + \mathrm{e}^{-} + \bar{\nu}\,, \tag{1.5}$$

$$\mathrm{p} \rightarrow \mathrm{n} + \mathrm{e}^{+} + \nu\,, \tag{1.6}$$

$$\mathrm{p} + \mathrm{e}^{-} \rightarrow \mathrm{n} + \nu\,, \tag{1.7}$$

where n is a neutron, p is a proton, e^{-} is an electron, e^{+} is a positron[1], ν is a neutrino[2], and $\bar{\nu}$ is an antineutrino.

[1] Positron is the antiparticle of the electron. It has the same mass and spin as the electron, but an opposite (positive) electric charge.

[2] Neutrino is a fundamental particle belonging to the lepton family, with no electric charge and tiny mass. It interacts only through the nuclear weak force and gravity, making it extremely difficult to detect.

The first case is the β^- **decay**, where a neutron is transformed into a proton and an electron and an antineutrino are emitted. This process generally happens in a neutron-rich nucleus. The second case is the β^+ **decay**, where a proton is transformed into a neutron and a positron and a neutrino are emitted. This process usually happens in a neutron-deficient nucleus. The third case is **electron capture decay**, where a proton inside a neutron-deficient nucleus captures a K-electron from its atomic shell, transforming into a neutron and emitting a neutrino [5, 38].

1.2.2 Channeling Concepts

Channeling occurs when charged particles traveling through a crystal lattice undergo a series of small, correlated deflections due to their interaction with the screened Coulomb potentials of the atomic nuclei arranged in periodic rows or planes. It can occur with many types of charged particles, such as ions, electrons, etc. The basic mechanism can be understood by considering the simplest case of channelling, namely axial channelling along a chain of atoms. In this case, we consider a beam of electrons, which are negatively charged particles, moving along the atomic chain. The projectiles oscillate around the chain, where the Coulomb potential reaches a minimum due to the attractive interaction between the negatively charged electrons and the positively charged nuclei. As a result, the electrons are guided through the channel while they penetrate the crystal [39, 40]. This is illustrated schematically in the following figure (1.9):

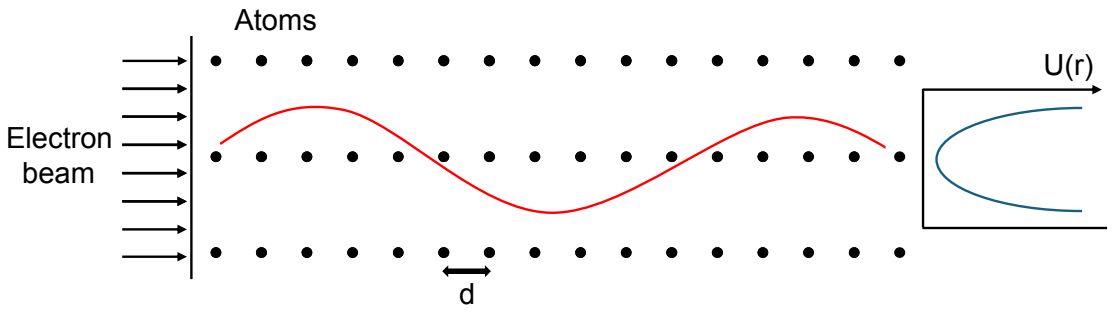

Figure 1.9: Schematic representation of the path of an electron and the corresponding electric potential. The vertical axis represents the position, and the horizontal axis the electric potential in a continuum model.

The **continuum approximation** treats the crystal as continuous rows or planes of atoms rather than discrete atoms. This helps explain how electrons move at small angles along a row of atoms become guided along the chains of atoms. While this model gives a useful general understanding of channeling, it oversimplifies some details like lattice vibrations

and exact atomic positions. More accurate methods, such as Monte Carlo simulations, are available but less intuitive. Besides that, when we are studying electron emission channeling we need to use **quantum treatment** despite the high particle energies (where the emitted particles are electrons and positrons).

The electronic potential shown in Fig.1.9 represents the continuum approximation of the screened Coulomb potential[1] at a distance r, as given below:

$$U(r) = \frac{Z_1 Z_2 e^2}{4\pi\varepsilon_0 d} \ln\left[\left(\frac{Ca}{r}\right)^2 + 1\right] , \tag{1.8}$$

where Z_1 and Z_2 are the atomic numbers of the projectile and the crystal atoms, respectively. e is the electric charge, ε_0 is the permittivity of free space, d is the distance between atoms in the same row, a is the Thomas-Fermi screening radius, and C is a constant ($C \approx \sqrt{3}$) [39, 40].

Simulations are therefore performed using the many-beam dynamical theory. This approach considers the electron wavefunction as composed of two components: a relativistic part, governed by the Klein-Gordon equation, describing motion along the channeling axis; and a perpendicular component, described by Bloch waves, which result from solving the Schrödinger equation in a periodic potential which is composed of Doyle-Turner atomic potentials for each atom. The number of beams in this model corresponds to the number of Bloch waves considered. A detailed description of the classical vs quantum treatment of channeling goes beyond the scope of this thesis and can be found e.g. in [5, 40].

The channeling effect depends strongly on the direction of the beam relative to the channeling axis. A critical angle can be defined such that, if the angle of incidence exceeds this value, channeling does not occur. This critical angle is known as **Lindhard's critical angle** [39], which is defined as:

$$\psi_c = \sqrt{2Z_1 Z_2 e^2 / Ed} , \tag{1.9}$$

where E is the kinetic energy of the projectile. A detailed derivation of this angle can be found in [5].

[1] The screened Coulomb potential describes the reduction in the effective interaction between charged particles due to the screening effect of atomic electrons surrounding atomic nuclei.

Lindhard's reciprocity theorem establishes a fundamental equivalence between channeling effects observed when charged particle beams enter a crystal from the outside and channeling effects related to charged particles emitted from sources inside the crystal. This theorem is crucial in understanding and interpreting emission channeling and blocking[1] experiments, as it allows one to treat the two scenarios as equivalent under certain conditions (mainly that irreversible processes like energy loss due to electron scattering are negligible). Practically, this means that experiments with external beams can be directly compared to emission channeling experiments with internal emitters, provided the emitters are not too deep inside the crystal [5, 40, 41].

The theorem also greatly simplifies **numerical simulations**, since it is more efficient to model particle tracks entering from outside than to simulate their trajectories starting inside the crystal.

It should be noted that this concept also applies to positively charged particles. However, instead of traveling along the atomic chains, these particles move between two chains, where the Coulomb potential is minimised. This is because positively charged particles are repelled by the atomic nuclei, in contrast to negatively charged particles, such as electrons, which are attracted toward the atomic nuclei, described in more detail in [39].

1.2.3 Electron Emission Channeling with Radioactive Isotopes

The type of emission channeling used in this study is electron emission channeling from implanted radioactive isotopes (probes). Experimentally, a sample is implanted with the appropriate isotope to study a particular chemical species. This technique allows us to **determine the lattice sites** of the isotopes by exploiting the fact that the emission yield of charged particles from the surface varies strongly with crystal orientation, depending on the emitter's position in the lattice. The implanted isotopes act as sources of charged particles, such as β^-, β^+, and conversion electrons, which, when emitted along high-symmetry directions, may be channeled or blocked by the crystal structure, leading to angle-dependent variations in the measured yield.

Figure 1.10 illustrates how particle yield anisotropy, influenced by channeling and blocking effects, can be used to determine the lattice site of a radioactive probe in a typical electron channeling experiment. It shows that when the probe occupies substitutional sites, the emitted electrons undergo channeling along all crystallographic directions. In

[1] Blocking is the opposite of channeling. It occurs when particles are not guided along the channel axis and therefore cannot pass through the channel.

contrast, interstitial site occupation leads to either channeling or blocking, depending on the observed crystal axis. The example emphasises the importance of measuring along several complementary directions to identify the probe's lattice location unambiguously.

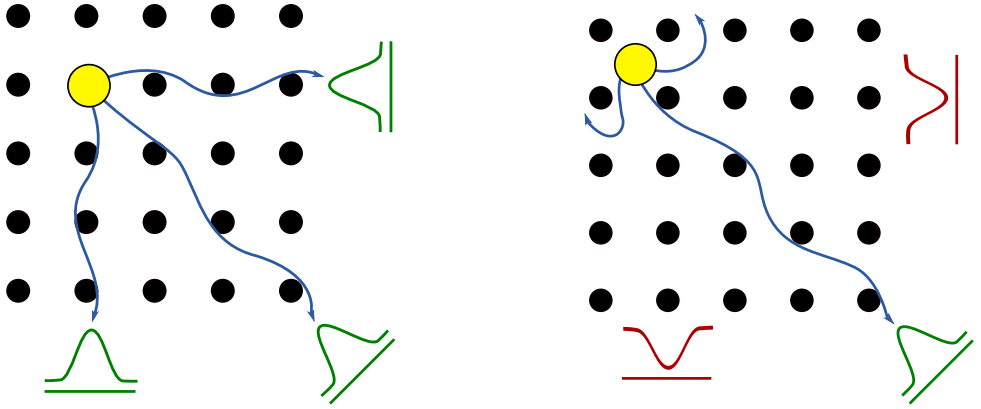

(a) Substitutional probe. (b) Interstitial probe.

Figure 1.10: Two-dimensional schematic representation of the channeling behaviour of electrons from a radioactive probe located at two distinct positions in the crystal lattice.

The angular emission yield anisotropy is currently measured using a two-dimensional (2D) position-sensitive detector (PSD) placed 30–60 cm from the sample implanted with a radioactive probe. The sample is mounted on a high-precision goniometer, allowing the positioning of its principal crystallographic axes to be aligned toward the detector. Angular distributions of the emitted particles are acquired for a set of complementary crystal orientations.

These measured distributions are then fitted using simulated libraries specific to the particle type, its energy spectrum, and the implantation conditions. The simulations predict angular emission yields for a wide range of possible lattice sites the probe may occupy. By comparing the experimental data to the simulated patterns, both the lattice sites and their respective occupancy fractions can be identified.

The EC-SLI (Emission Channeling with Short-Lived Isotopes) collaboration, to which this work belongs, is a collaborative effort primarily between the Instituto Superior Técnico (IST) and the Belgian University of KU Leuven (Quantum Solid-state Physics group - QSP). The three off-line experimental setups, as well as the on-line EC-SLI setup, are located at ISOLDE (CERN), where emission channeling experiments using 2D position-sensitive detectors have been conducted since 1996 [42, 43]. The Institute of Physics for Advanced Materials, Nanotechnology and Photonics of the University of Porto (IFIMUP) has maintained collaborations and funded projects with these research units for several years, which enabled the development of the present work.

An important parameter in emission channeling simulations is u, the root-mean-square (rms) displacement of an atom from its equilibrium position. This parameter is used in the thermally averaged Doyle-Turner potential to model the crystal, thereby influencing both the electronic energy levels and the dechanneling effects caused by thermal vibrations of the lattice atoms, deviations from the ideal periodic structure [5].

The values of u for the host crystal atoms are typically taken from the literature. For impurity atoms, the value is often estimated, although larger values can also be considered to represent broader Gaussian distributions than those resulting from purely thermal vibrations.

Simulated patterns depict a normalised yield, defined relative to the yield expected in the absence of channeling, such as in an amorphous material. Directions at which this normalised quantity is close to unity are referred to as random directions, and a uniform distribution of yield across all directions is termed a random pattern. Experimental data generally include a contribution from such a random pattern, which is always considered during fitting. This random component functions similarly to a constant offset in linear regression and may originate from various sources such as background radiation, incoherent electron scattering, amorphous regions in the sample, or a uniform, i.e. random distribution of emitting sites within the crystal.

During the fitting process, instrumental broadening affecting the angular resolution must also be accounted for. These arise from the finite resolution of the PSD, denoted σ_{detector}, and the finite size of the implantation beam spot, σ_{spot}. These effects are incorporated through a Gaussian smoothing function with an effective one-dimensional standard deviation σ, calculated as:

$$\sigma = \arctan\left(\frac{\sqrt{\sigma_{\text{detector}}^2 + \sigma_{\text{spot}}^2}}{d}\right) \tag{1.10}$$

where d is the distance from the sample to the detector [5, 44].

The fitted fractions, including the random component, sum to unity. However, the random fraction typically includes contributions from background radiation and scattered electrons within the measurement chamber. To isolate the true random contribution, corrections can be made by estimating the background through separate measurements or simulations. These corrections are subject to uncertainties and typically result in absolute sum site

fraction errors of about 10% [45].

1.2.4 Decay of ^{24}Na

In this work, we use ^{24}Na, a neutron-rich unstable isotope of sodium, as a radioactive probe with a half-life of about 15 hours. It decays into ^{24}Mg, a stable isotope of magnesium, via the emission of β^- particles, as shown in Fig.1.11. While the emission is isotropic with respect to the decay site, the emitted charged particles interact with the diamond lattice, undergoing channeling along its crystallographic planes and axes, which gives rise to the emission channelling patterns.

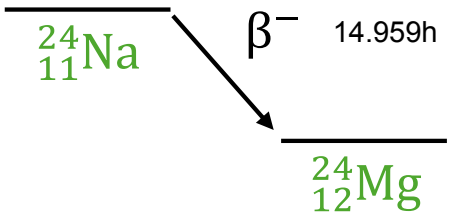

Figure 1.11: Decay scheme of ^{24}Na.

In Fig.1.12, we show the energy spectrum of the β^- decay of ^{24}Na. This spectrum was produced using data from the Nuclear Energy Agency (NEA) JANIS database [46]. As can be seen, the energy spectrum is very broad, with some particles emitted with only a few keV, and although the spectrum extends up to 4114 keV, there is practically no electron intensity above 1400 keV. The mean energy is 556.2 keV, which corresponds to the most frequently observed energy of the emitted β^- particles.

The reason why the energy spectrum is continuous and broad, rather than consisting of one or two discrete lines, is that β^- decay involves three particles: the proton, the electron, and the antineutrino. Due to this three-body interaction, conservation of momentum and energy results in a continuous distribution of energies among the emitted particles.

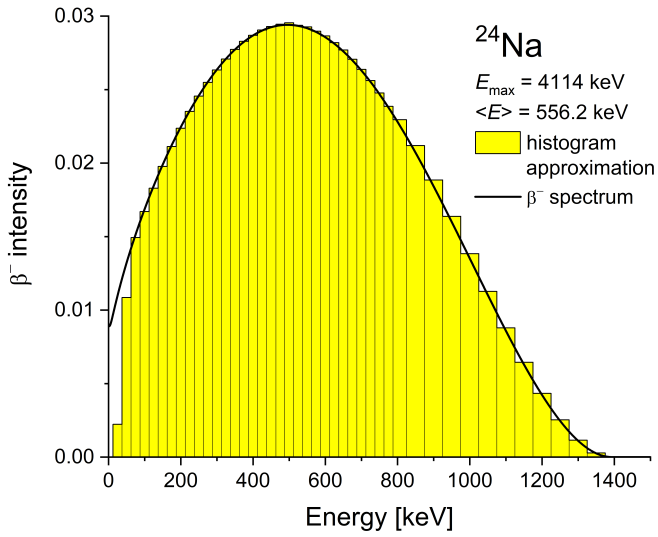

Figure 1.12: Energy spectrum of the β^- decay of ^{24}Na.

In quantum technology applications, the relevant form of sodium is the stable isotope ^{23}Na, which is the only stable isotope of sodium. However, to determine the lattice site of sodium using the emission channeling technique, a radioactive isotope is required. For this reason, ^{24}Na is chosen, as it undergoes β^- decay, emitting electrons suitable for the technique. Despite differing by a single neutron, ^{23}Na and ^{24}Na are chemically identical, and it is a reasonable assumption that they occupy the same lattice sites in the crystal when forming impurity defects.

1.3. ISOLDE/CERN

The European Organisation for Nuclear Research, commonly known as **CERN**, is an intergovernmental organisation that operates the world's largest laboratory for particle physics. Founded in 1954, CERN is situated in Meyrin, a suburb of Geneva, located on the border between France and Switzerland. It currently has 25 member states [47].

CERN is home to the Large Hadron Collider (**LHC**), the most powerful particle accelerator ever built. In the LHC, protons are accelerated to near the speed of light and smashed together to recreate conditions similar to those just after the Big Bang. These experiments help physicists explore the basic structure of matter [47]. One of CERN's major achievements was the discovery of the Higgs boson in 2012, a key particle that explains how other particles acquire mass [48]. CERN is also known for inventing the World Wide Web in 1989, originally developed to help scientists share information [49]. Beyond these, CERN

contributes to advances in technology, computing, and medical imaging, while pushing the boundaries of our understanding of the universe.

CERN hosts a wide range of facilities and accelerators that make experiments at the LHC and its predecessors possible (Fig.1.13). Approved by the CERN Council in 1964, the ISOLDE facility (Isotope Separator OnLine DEvice) received its first beams in 1967. Later, in 1992, the facility was redesigned, allowing it to take advantage of the existing high-energy proton beam and re-enabling the production of radioactive ion beams (RIBs) for diverse studies in nuclear, particle, and solid-state physics [47].

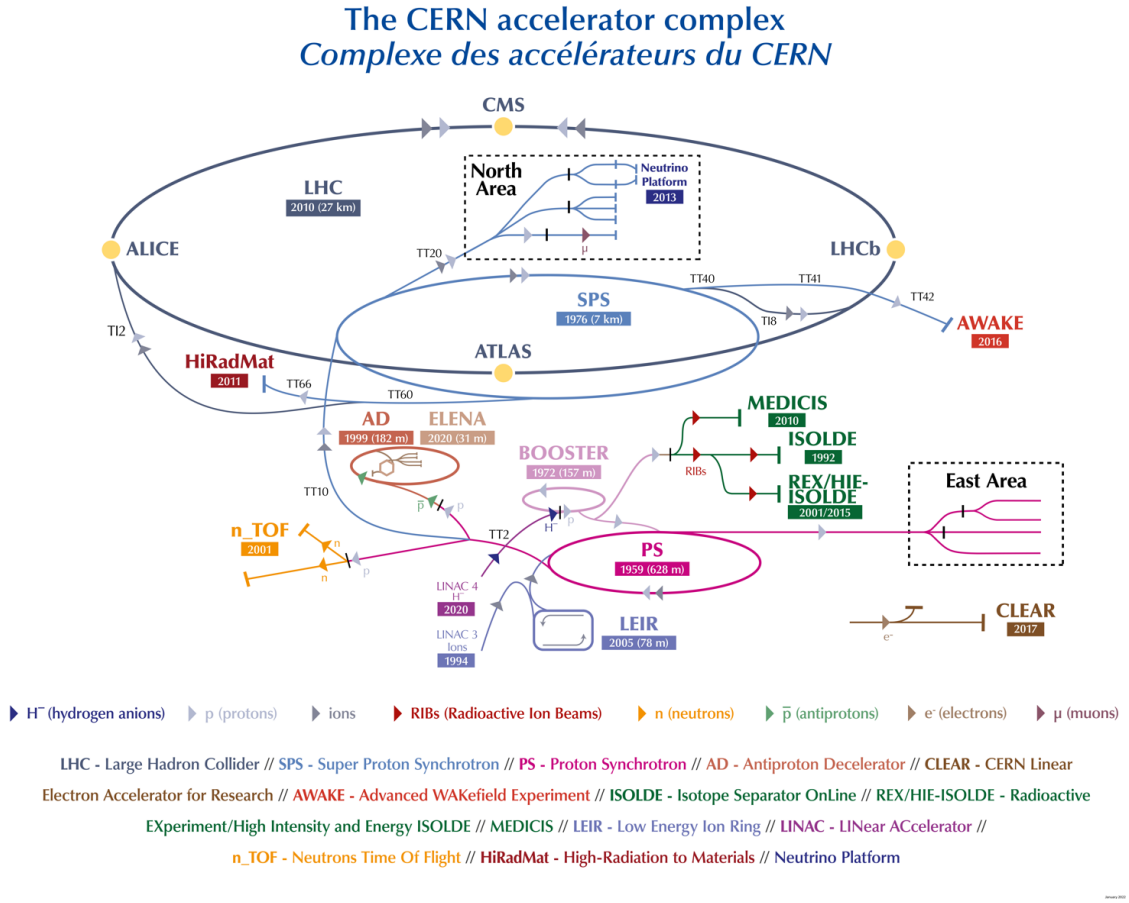

Figure 1.13: CERN facilities with their opening year and the length of the accelerators [50].

1.3.1 Production and implantation of radioactive isotopes

For electron emission channeling (EC) experiments, radioactive isotopes must first be produced and then implanted into a single-crystal sample via ion implantation. This process is illustrated by the facility layout shown in Fig.1.14.

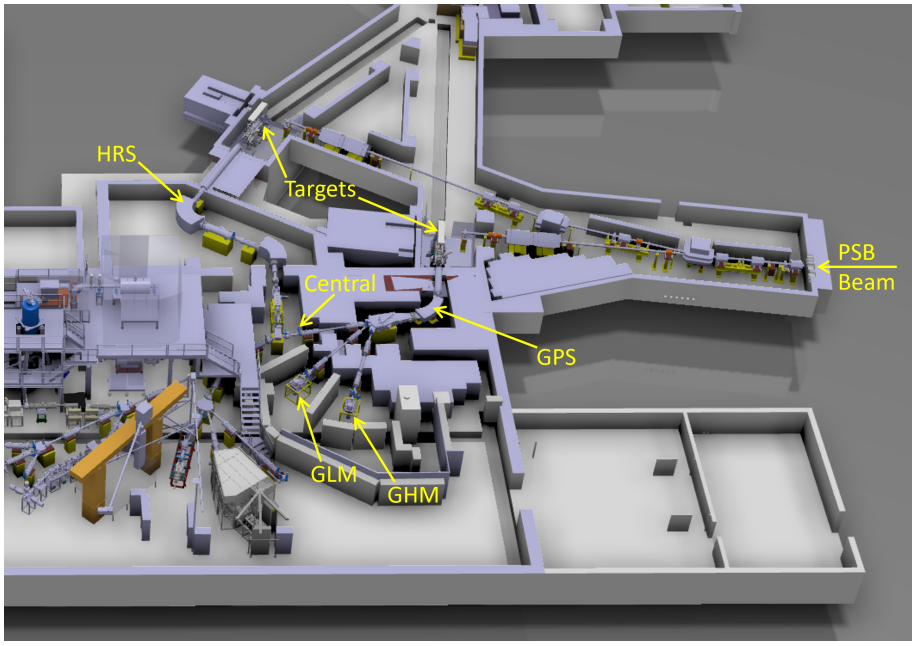

Figure 1.14: General layout of the ISOLDE facility [51].

As mentioned earlier, ISOLDE receives a high-energy proton beam from the Proton Synchrotron Booster, the second stage of acceleration for the LHC. The beam has an energy of 1.4 GeV and a maximum current of 2 μA of single charged ions. Upon arrival, it is directed to one of two targets, each coupled to its mass separator: the General Purpose Separator (GPS) or the High Resolution Separator (HRS). These separators use large analising magnets with high mass resolution, used to select specific isotopes based on their charge-mass ratio [52]. After passing through the GPS, the isotope beam can be directed to either the General High Mass (GHM) or the General Low Mass (GLM) beam line. Emission channeling experiments are conducted in the GHM area, while the GLM is typically used for implantation or other types of experiments. The central beamline is reserved for other experimental setups within the ISOLDE facility.

The majority of targets consist of heavy elements or their compounds, such as ^{238}U (Uranium Carbide); however, the elemental composition may vary depending on the specific isotope being produced. When struck by the proton beam, the heavy nuclei undergo nuclear reactions - fission, fragmentation, or spallation - resulting in the production of a wide variety of radioactive isotopes. To facilitate isotope release, such targets are heated to temperatures between 1500-2000°C using a high current of around 900 A [53].

Ionization of the produced isotopes can be achieved through three main techniques: surface ionization (for which purpose it was used in this work to produce Na beams), which

involves heating metallic surfaces at the target's exit so that atoms lose electrons upon collision - effective mainly for elements with low ionization potential like alkali metals and some rare earths; plasma ionization, where isotopes pass through a plasma discharge with low element selectivity; and laser ionization, which uses tuned lasers to selectively ionise specific elements. Laser ionisation at ISOLDE is performed using the Resonance Ionisation Laser Ion Source (RILIS) [53, 54]. Once ionised, the ions are accelerated to energies of up to 60 keV, forming Radioactive Ion Beams (RIBs) that are directed to the experimental beam lines. At the end of the beam line, the radioactive ion beams are implanted into the samples for further analysis [52]. For short-lived isotopes, with half-lives on the order of a few hours or less, the emission channeling measurements must be performed in *situ*, using the **on-line setup** in a chamber that is attached to the GHM beam line. For very short-lived isotopes (e.g. half-lives of the order of seconds), the measurements are performed on-line during implantation. In contrast, long-lived isotopes can be safely transported in lead-shielded containers to a dedicated laboratory within the ISOLDE complex, where three additional emission channeling setups, referred to as **off-line setups**, are available for further studies.

2. Experimental Methods

2.1. Emission Channeling

2.1.1 Set-up description

Fig.2.1 shows a schematic vertical cross-section of the experimental on-line set-up, where the ion beam from ISOLDE enters from the left. In the first chamber, the beam encounters the Collimator Chamber, where a laser is used to align the set-up after interventions or to verify proper alignment when needed. A collimator shapes the incoming beam. After passing through the collimator chamber, the beam reaches a second collimator at the entrance of the main chamber, known as the ”nozzle”, which collimates the beam to a diameter of 1 mm. Here, the beam can either hit the sample or be directed to a Faraday cup, depending on whether the sample holder is moved upwards to allow the beam to pass through to the Faraday cup. When the sample holder is moved up, the Faraday cup measures the ion current, which is later used to calculate the implantation fluence.

The set-up also includes a vacuum system, composed of a rotary pump and a turbo-molecular pump, responsible for establishing the primary and secondary vacuum levels, respectively (down to approximately 1×10^{-6} mbar). Additionally, the system also contains the components necessary to perform thermal annealing. These allow the sample to reach temperatures of up to 900°C. A halogen lamp is also included to provide illumination, allowing visibility inside the chamber.

The sample holder is mounted on a high-precision goniometer, which enables accurate alignment of the crystal axes relative to the detector. The available degrees of freedom include translational movement along the x, y, and z axes, as well as three rotational motions: M1 (rotation around the vertical axis), M2 (rotation around the sample normal), and M3 (rotation around a horizontal axis perpendicular to the sample normal). Typically, the translational motions and M3 are set at the beginning of the experiment, with only M1 and M2 being used for fine alignment and axis switching during measurements.

The detector is positioned at an angle of 17º to the right in the plane of the beam. In this position, the detector can be replaced with other detectors. A valve isolates the detector from the chamber to protect it from external light exposure and from potential damage caused by high-temperature radiation during annealing.

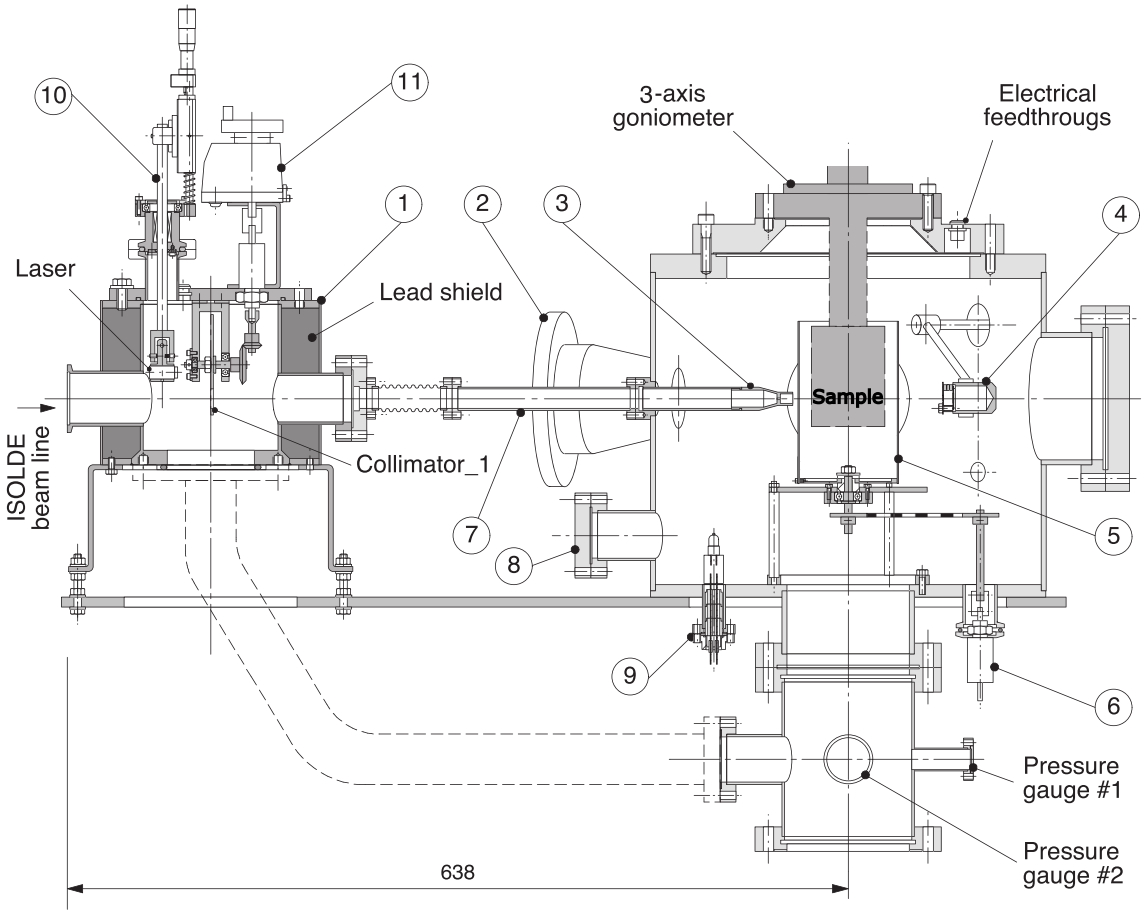

Figure 2.1: Emission Channeling set-up vertical cross section: 1 - collimator chamber with lead shield, rotatable disk with collimator holes, alignment laser; 2 - detector flange DF17; 3 - fixed aperture removable collimator; 4 - movable Faraday cup; 5 - revolving thermal shield; 6 - thermal shield actuator; 7 - ion beam transport tube; 8 - spare flange; 9 - halogen lamp; 10 - alignment laser mechanism; and 11 - Collimator_1 wheel rotation mechanism [55].

Fig. 2.2 shows photographs of the EC set-up. In Fig.2.2 (a), we can see the main chamber where the samples are implanted and measured, and the left lid-door used for changing the samples. The equipment above the main chamber is the high-precision goniometer, together with the respective knobs that allow us to rotate the sample to orient it. We can also see the beamline coming through the wall, which carries the radioactive sodium beam, in our case. Fig.2.2 (b) was taken during the annealing process through the right window (which is not visible in the left picture). This is why the sample appears to be emitting a red colour, as it is at high temperature (900°C). We can also see the nozzle through which the radioactive beam enters, the halogen lamp at the bottom (turned off), and the sample holder mounted on the goniometer. The various cables are used to measure electrical currents in the Faraday cup, supply current to the heating element, and read the thermocouple voltage for temperature measurement. The Faraday cup shown

in Fig.2.1 is hidden at the bottom left so that it does not collide with the sample holder.

(a) Left-front view of the set-up.

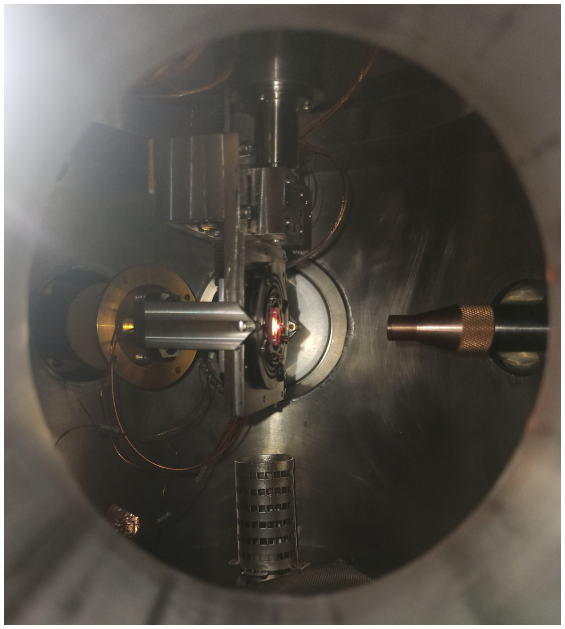

(b) View inside the chamber through the right window during the annealing process of the sample.

Figure 2.2: Photographs of the emission channeling set-up.

2.1.2 Experimental procedures

The procedure begins by mounting the sample onto the support that fits into the sample holder. Using the goniometer handles, the sample holder is then rotated so that it faces the load lock door of the chamber, allowing the sample to be properly inserted. Once in place, the sample is rotated until it is aligned with the beam entrance. Before starting data acquisition, a background signal measurement should be performed. The beam is then directed to the desired spot on the sample, and implantation continues until the target fluence is achieved. To cover a crystallographic axis, the sample is moved accordingly. Measurements can be taken either during (if the temperature is below 800°C) or after the implantation process. If data from another crystallographic axis is required, the position or inclination of the sample is adjusted, and acquisition is repeated. If necessary, the sample can be annealed (with a typical duration of 10 minutes) before repeating the entire procedure.

2.2. Photoluminescence

2.2.1 Set-up description

Fig.2.3 shows a schematic diagram of the PL spectroscopy set-up, consisting of two excitation laser sources, an XYZ translation stage, mirrors, filters, shutters, a fibre coupler, and a spectrometer. The traces of the lasers are shown in green and blue, the luminescence light is represented in yellow, and the fibre optic link is shown in purple.

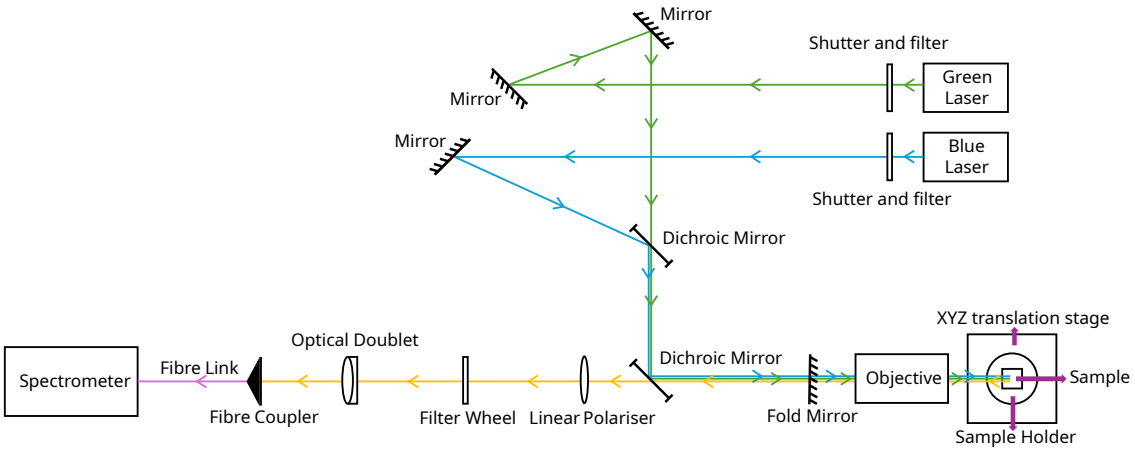

Figure 2.3: Schematic diagram of the photoluminescence set-up.

Fig.2.4 shows photographs of the PL set-up. In Fig.2.4 (a), we see a picture taken from the same perspective as the schematic diagram shown above, including the traces of the lasers and the luminescence light. In Fig.2.4 (b), we have a frontal, slightly elevated view, where the XYZ translation stage, the objective, and the sample holder are visible. The objective itself partially covers the sample in this picture. It is also clear how the fold mirror redirects the light path from the horizontal plane to the vertical one, and then focuses it onto the sample.

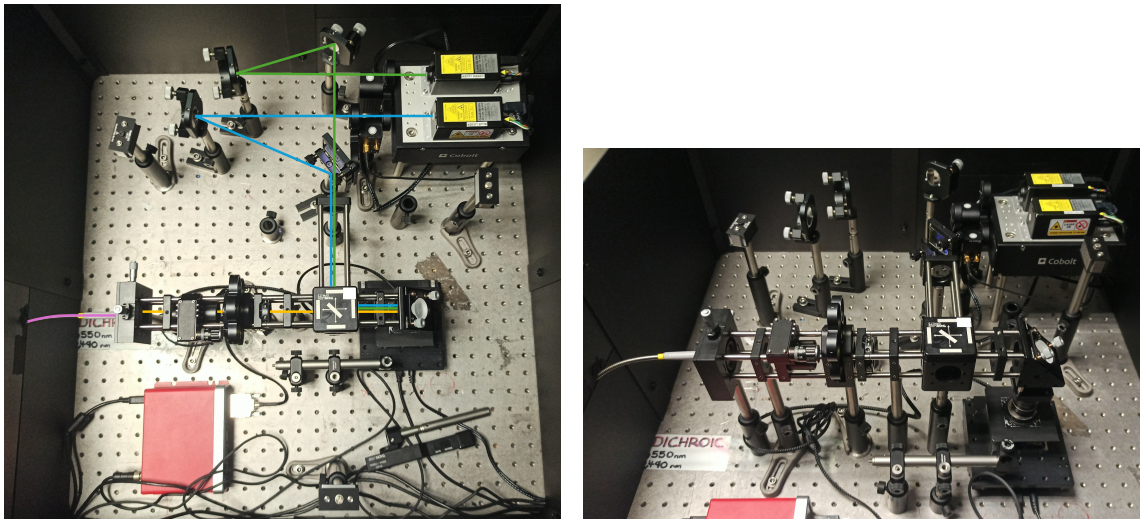

(a) Top view of the set-up, matching the schematic diagram perspective.

(b) Frontal, slightly elevated view of the set-up.

Figure 2.4: Photographs of the photoluminescence set-up from two different perspectives.

In this experimental set-up, two lasers are used: a green laser with an emission wavelength of 532 nm (Cobolt 06-DPL 25mW) and a blue laser at 457 nm (Cobolt 08-DPL 30mW). We chose these DPL lasers because of their high frequency and power stability, as well as low divergence. These allow selective excitation of different defects by choosing the appropriate laser source. In front of each laser, a motorised shutter and filter module is installed. The shutter allows the beam to be blocked without turning off the laser, which helps maintain its thermal and power stability. When the shutter is open, the beam passes through a bandpass filter with a ± 5 nm window centred on the laser's wavelength, ensuring a well-defined excitation energy. The filters used were FBH460-10 and FBH530-10 for the blue and green lasers, respectively. To properly direct and focus the beams, each laser path requires at least two adjustable mirrors. For the green laser, two standard silver-coated mirrors with 95% reflectivity (PF10-03-P01-10) are used. For the blue laser, a standard mirror is combined with a dichroic mirror (DMLP505R), which reflects blue light from one side while transmitting green light from the other.

The next dichroic mirror directs each beam into its corresponding optical path, using either the blue (T470lpxr) or green (RT532rdc) dichroic, depending on which laser is utilised for excitation. The beam is subsequently reflected by a fold mirror (BB1-E02, a dielectric mirror with 99.5% reflectivity) that redirects the light from the horizontal plane of the optical table into a vertically mounted microscope objective (MPLAPON100X) with a numerical

aperture (NA) of 0.95 and a magnification of 100×, which focuses the beam onto the sample. The sample is mounted in a holder attached to an XYZ translation stage: XY motion is controlled by servo motors, while Z positioning is achieved via a piezo actuator, which offers significantly higher sensitivity than the servo motors, enabling precise movement at the micron and sub-micron scale.

Upon excitation, the defects emits light at a different wavelength. This photoluminescence light travels back along the same optical path but is now transmitted through the dichroic mirror. It then passes through a linear polariser (WP25M-VIS), which helps suppress Raman scattering lines due to their strong polarisation dependence. The signal then passes through a long-pass filter mounted on a motorised filter wheel, which blocks any reflected excitation light. For the blue laser, an ET460lp filter is used, with a cutoff wavelength of 460 nm. For the green laser, an RET537lp filter is used, with a cutoff at 537 nm. Different filters are used for the green and blue lasers, and the appropriate one is selected by rotating the wheel.

Finally, the filtered emission is focused onto the entrance of an optical fibre using an optical doublet lens (ACA254-050-A) and coupled into the fibre with a fibre coupler. The doublet lens reduces aberrations compared to a typical convex lens. The light is guided through the fibre to an iHR 550 spectrometer with a 600 lines/mm grid, where the optical spectrum, intensity (counts) versus wavelength, is captured by the Horiba Symphony CCD3000 camera.

2.2.2 Experimental procedures

The sample should be mounted with the implanted side facing upward and inserted into the XYZ translation stage. To locate the focal plane, one has to use the green laser first, as it provides better visual feedback for focus adjustments. Because the sample has a slight slope along the X direction, the focus should be checked at two opposite ends along this axis to determine how the focal plane shifts with position. The slope in the Y direction is negligible and can be ignored.

One must choose the laser type according to the sample and the nature of the experiment. Initially, acquire spectra at different wavelengths to search for any detectable signal. If a signal is observed that might be related to sodium-related defects, a Z-scan (depth profiling) should be performed to determine whether the emission originates from the surface or from deeper within the sample. Due to the ion implantation process, which produces

sharply defined and narrow impurity or defect profiles near the surface of the sample (e.g. an implantation depth of 480 Å and a straggling of 144 Å for 50 keV ^{24}Na), a peak-like response is expected that reflects the depth resolution function of the experimental setup (with a FWHM (Full Width at Half Maximum) on the order of 10 µm), as will be demonstrated also by our results, e.g. Fig.3.6.

Note that our PL set-up, while it has depth resolution, is not strictly a so-called ”confocal” setup, which can provide depth resolution down to the diffraction limit (a few tenths of a micrometre). A confocal setup would require that the last doublet lens focus the light through a small pinhole. In our case, the entrance of the fibre optics acts as the equivalent of a pinhole, though with a larger diameter and hence providing worse depth resolution.

Following this, an XY-scan across the entire sample area should be conducted to map the spatial distribution of the suspected defects and compare it with the expected implantation pattern. Once regions of interest have been identified, the full emission spectrum should be recorded. To acquire the **XY and Z-scans**, we used a **LabVIEW** (commercial software developed by National Instruments) programme created by Zeno Maesen and Kirill Danilov from the Belgian university of KU Leuven. The PhD student Kirill Danilov also collaborated on these experiments. In addition to these scans, the programme also allows us to record standard spectra as a function of wavelength and to monitor the CCD (Charge-Coupled Device) temperature.

For an XY-scan, we first select the starting position, typically at the bottom left of the sample, and define the number of steps and step size according to the desired resolution. The scan proceeds line by line from left to right, moving up one line each time until it is complete. Next, we configure the spectrum to be acquired, specifying the central wavelength (CW), the aperture width (APT), the exposure time (ET), balancing resolution and the amount of light collected, and the number of signal averages (AVG). We then select the integration windows by setting its central wavelength and width, and optionally activate background correction by choosing a background window. The programme integrates these windows using the trapezoidal rule and calculates the ratio $(\text{signal} - \text{background})/\text{background}$, which can yield negative values if the background exceeds the number of photons collected in the signal window.

During an XY-scan, the main variables changing are the x and y positions. However, since the sample surface has a slope, maintaining focus requires compensating for this inclination. By determining the slope of the focus along the x-axis, we can instruct the

programme to adjust the z position accordingly.

Acquiring a Z-scan is similar, but instead of scanning a region, we choose a fixed position and vary the z coordinate. For safety reasons (to avoid accidentally hitting the sample), our z-scans are implemented such that they start at a chosen minimum z-value, which is then successively increased by moving the sample away from the objective.

To acquire our data, we used the **SynerJY** programme from HORIBA Scientific, as it offers specific functionalities, such as real-time acquisition that allows us to see what we are acquiring without saving the data. The acquired data are plotted within SynerJY using the commercial graphics software Origin. To acquire a spectrum with SynerJY, we need to choose the central wavelength (CW), the aperture width (APT), the exposure time (ET), and the number of signal averages (AVG) or, alternatively, the number of unsummed spectra forming a stack (STK). We can also use the range function, in which the programme automatically changes the CW to cover the desired spectral range. Additionally, the software displays the temperature of the CCD.

We used liquid nitrogen to cool the CCD camera. Its temperature should be around 136 K (-137.15°C). If the temperature starts to rise, we need to refill it before starting the acquisition.

3. Results and Discussion

3.1. Emission Channeling

In this work, we measured two different samples of ^{24}Na, both implanted into SC diamond at room temperature. The first sample, #530, was implanted at an energy of 50 keV with a fluence of 2.8×10^{13} atoms/cm^2, and the implantation lasted 43 minutes. The second sample, #565, was implanted at 30 keV with a fluence of 5×10^{12} atoms/cm^2, for 11 minutes. Both implantations were performed at an angle of 17º from the surface normal and resulted in approximately Gaussian depth profiles, with implantation depths and straggling of 480 (144) Å for 50 keV and 293 (95) Å for 30 keV [56].

A position-sensitive silicon pad detector with 22×22 pixels, each measuring 1.3×1.3 mm^2, was used and placed 30 centimetres from both samples.

EC experiments in crystals of the diamond structure are usually performed by studying the emission anisotropies around the $\langle100\rangle$, $\langle110\rangle$, $\langle111\rangle$, and $\langle211\rangle$ axes, which are the crystallographic directions of highest symmetry. It is also essential to acquire background data between measurements with the detector valve closed.

Once the crystallographic direction has been chosen, data acquisition proceeds until the detector registers sufficient statistics for meaningful analysis, which in this case was considered to be around one million events, or above roughly 2000 counts/pixel. During acquisition, it is important to monitor the emerging pattern to identify any evidence of channelling. If no channelling effect is observed, the direction should be adjusted. In this experiment, we aimed to measure the angular patterns along the $\langle100\rangle$, $\langle110\rangle$, $\langle111\rangle$, and $\langle211\rangle$ crystallographic directions for both samples. These four orientations should allow us to determine the lattice site occupied by the ^{24}Na atoms. We repeated these measurements after annealing the sample at 300°C, 600°C, and 900°C for 10 minutes each, in order to investigate how the defect configuration evolves with temperature.

To extract the possible lattice sites and their respective occupation fractions responsible for a given pattern, the experimental data must be fitted by a library of simulated patterns. In this work, a pre-computed library was used, containing patterns within a ±3º angular range, with steps of 0.025º along both angular axes for each selected crystallographic direction. The simulated library also includes patterns accounting for atomic displacements, with positions shifted from one lattice site towards another. These displacements were

applied in steps of either 0.05 or 0.1 units (0.1 units is around 0.04-0.08 Å), with finer 0.05 steps used in cases where higher precision was necessary.

The experimental patterns were fitted using the **JavaFDD** software [44]. Java is the programming language in which the software is written, and **FDD** stands for the fit done in two dimensions. This technique is used to identify the lattice site of implanted atoms by fitting experimentally measured angular distribution patterns with a precomputed library of simulated patterns. JavaFDD performs this comparison using routines based on non-linear least square minimisation [44].

Due to the presence of dead pixels on the detector, a mask was applied to exclude these pixels during the fitting process. The software allows the user to specify the number and types of lattice sites to be fitted. In addition to the occupation fractions, it also fits the xy-coordinates of the centre of the pattern and its azimuthal rotation angle, as well as a scaling factor. It begins with an initial guess and then uses iterative algorithms to minimise the fitting error. The error function employed in the software is the reduced chi-square, χ^2_{red}. The chi-square, χ^2, is a quantity that characterises the difference between the experimental data and the fitted model. The reduced chi-square, χ^2_{red}, is the chi-square normalised by the number of data points minus the number of degrees of freedom in the fit, providing a measure of the goodness of fit [57].

To analyse the data, we initially performed 1-site fits using all simulated lattice sites and their corresponding displacements. We used a smoothing, σ, of 0.1º, calculated using Eq.1.10, and a root-mean-square (rms) atomic displacement from equilibrium, u, of 0.044 Å, for the ^{24}Na emitter atoms. This value can be approximated to that found in [58] for the rms displacement of carbon atoms in diamond. Each annealing temperature yielded 4 experimental patterns, plus 4 from the unannealed sample, resulting in a total of 16 patterns for fitting for each sample.

After obtaining the fitting results, we searched for both global and local minima along each displacement path. We then verified whether the results had physical meaning, that is, whether the occupation fractions were positive and less than one. Fractions very close to one were discarded, as the presence of background counts must also be taken into account. Including such values would lead to a total fraction exceeding one, which is not physically meaningful.

From this initial fitting, we found that the best-fitting sites, in terms of lowest error and

agreement with theoretical predictions, were sites close to the substitutional (S) site. Based on this, we proceeded with 2-site fits, where we kept the first site fixed at the BC position and varied the second site (because the BC position is what would be expected if Na were found in the split-vacancy configuration), and then fixed the S site and varied the second site, following the same approach used in the 1-site fitting.

The best results were obtained with a combination of BC and S sites. We also attempted 3-site fits, fixing BC and S sites while varying the third site. However, these results were inconclusive, as many of the resulting fractions lacked physical meaning or showed no consistent trend in the error minimisation.

Fig.3.1 shows the simulated patterns for angular-dependent emission of beta-particles from ^{24}Na on substitutional and BC sites using the many-beam approach. There are 8 plots in total: the left column shows 4 plots corresponding to a 100% fraction of substitutional sites, while the right column shows 4 plots corresponding to a 100% fraction of bond-centre sites. The x and y axes represent the angles (in degrees) relative to the axial direction within the pattern. Note that the orientation of the patterns has been chosen to match the experimental patterns shown below in Fig.3.2. We plotted these patterns as heatmaps, where the colours represent the normalised β^- yield (in this case, the simulated yield). Blue indicates regions where the angular-dependent emission yield from the crystal is highest, i.e. where channeling effects occur for emission from the considered lattice sites, and red where it is lowest, i.e. where the normalised emission yield is close to one, or in case of blocking effects, even lower. Within the patterns, at the left edge, we can also see white areas where there are no results because the corresponding angles fall outside the $\pm$3º range of the simulations.

Before discussing the results, it is important to clarify what our **notation** means. As we can see, each plot is labelled with the crystallographic direction that was pointed towards the detector, denoted by angle brackets, for example, $\langle 110 \rangle$. Within the patterns themselves, we indicate the equivalent families of crystallographic planes, denoted by parentheses, for example, (111); this plane is perpendicular to the vector [111].

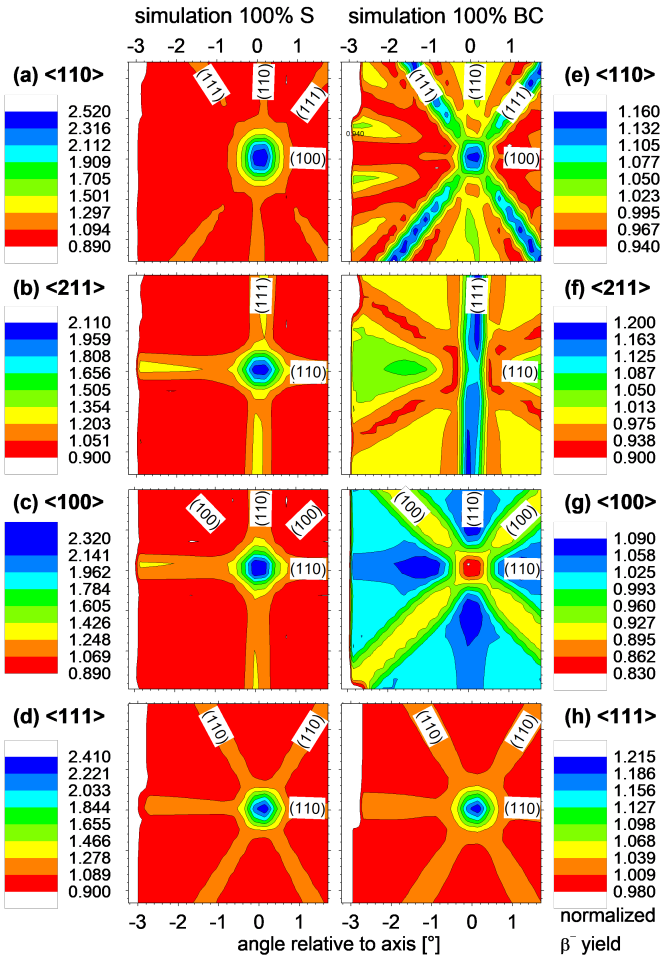

Figure 3.1: Simulated patterns for β^- channeling from ^{24}Na using the many-beam approach. On the left is the case with 100% fraction at the substitutional (S) site, and on the right is 100% fraction at the bond-centre (BC) site, both without any displacement. Note that the orientation of the simulated patterns has been chosen to correspond to the experimental results for sample #530.

Comparing the simulated patterns for the same crystallographic direction (i.e., within the same row of Fig.3.1), and considering the distances between carbon atoms in the diamond lattice (Fig.1.4), we can see that directions where atoms are further apart are less likely to exhibit channeling in the substitutional site. In the first row, plots (a) and (e), both for the $\langle 110 \rangle$ direction, correspond to a 100% substitutional site (S) and a 100% bond-centre site (BC), respectively. In the substitutional simulation, the direction where the channeling effect is most pronounced is along $\langle 110 \rangle$ it appears as a prominent blue circle near the centre of the pattern, followed by $\langle 111 \rangle$, $\langle 100 \rangle$, and then $\langle 211 \rangle$.

This is expected, as the strength of the channeling effect is roughly determined by the nuclear charge per unit length along the respective crystallographic direction of a substitutional site. In the diamond structure, the number of atoms per unit length along the

principal crystallographic axes is given by:

$$\begin{aligned}
\langle 100\rangle &: \frac{1}{a_0} = 1.000\, a_0^{-1}, \\
\langle 110\rangle &: \frac{2}{\sqrt{2}\, a_0} = 1.414\, a_0^{-1}, \\
\langle 111\rangle &: \frac{2}{\sqrt{3}\, a_0} = 1.155\, a_0^{-1}, \\
\langle 211\rangle &: \frac{1}{\sqrt{3/2}\, a_0} = 0.816\, a_0^{-1}.
\end{aligned}$$

As can be seen, the intensity of the axial channeling effects from substitutional (S) sites is roughly correlated with these values.

For the bond-centre simulation, the situation is qualitatively and quantitatively different from that of the substitutional case: first, the yield scale is notably smaller, i.e., the difference between the maximum and minimum yield (from blue to red) is only about 0.220, compared with around 1.630 for the substitutional sites. Unlike substitutional sites, which are always aligned with all atomic axes and planes, the bond-centre patterns may represent a mixture of projections, some aligned with the lattice and others interstitial with respect to the axes and planes, making it much harder to visualise the agreement between the simulated patterns and the diamond structure.

In Fig.3.2, we compare the experimental results after annealing at $T_a = 600$°C with the best-fit 2-site simulated patterns for each crystallographic direction studied. The angles in the experimental patterns were determined using the distance between the sample and the detector and the detector area. By taking the perpendicular line to the sample and detector as the reference axis, we computed the angle relative to this axis as the arctangent of the ratio between the pixel position and the sample-to-detector distance. For both samples, this distance was 30 cm; a distance of 60 cm could also have been used, which would reduce the angular range but improve the angular resolution.

The experimental patterns exhibit some background fluctuations due to the inhomogeneous response of the detector to gamma background radiation. We also observe that the scale, the difference between the maximum and minimum values, is quite small: approximately 0.230 for $\langle 110\rangle$, 0.180 for $\langle 211\rangle$, 0.100 for $\langle 100\rangle$,and 0.205 for $\langle 111\rangle$. The combination of site fractions in the best fit is a composition of 17% substitutional site and 51% bond-centre site. Despite this, we can be confident in our results, as the experimental

patterns closely resemble the best-fit simulations.

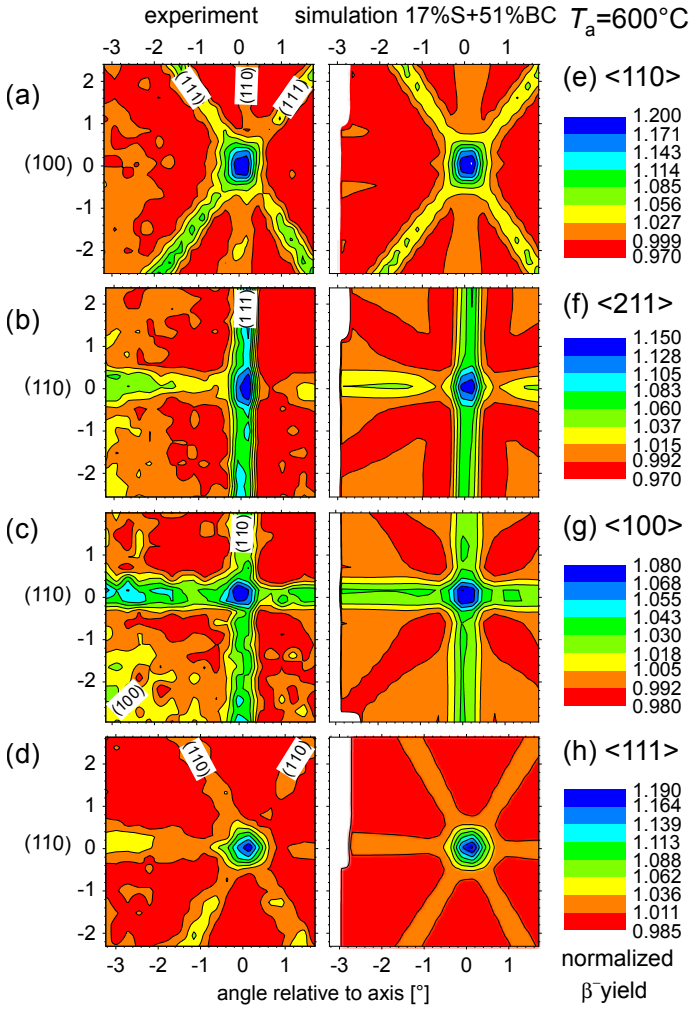

Figure 3.2: Comparison of experimental and best-fit simulated patterns after annealing at $T_a = 600$°C for sample #530.

The graphs and analysis for sample #565 are essentially similar, so it is not necessary to discuss them again as they show similar patterns and support similar conclusions.

In the last figure, after an annealing process at 600°C, we observed that the best 2-site fit corresponds to a mixture of 17% substitutional sites and 51% bond-centre sites for sample #530. However, it is important to investigate how these fractions vary with increasing annealing temperature, since the optical activation of implanted colour centres usually requires thermal annealing procedures.

In Fig.3.3, we present these fractions for all cases and both samples: at the top, sample #530, and at the bottom, sample #565. The measurements were taken for the unannealed sample ($T_a = 30$°C) and after annealing at 300°C, 600°C, and 900°C. The error bars shown for f_{BC} and f_S were calculated according to the standard deviation of the spread

of values derived from the patterns for the four different crystallographic directions. In the case of f_S, the error bars are smaller than the size chosen for the circles to represent the data points.

We also plotted the sum of the site fractions of the substitutional and bond-centre sites, $f_{\text{sum}} = f_{BC} + f_S$, to follow the overall tendency and to check whether some other type of site not accounted for might appear. If the sum decreases, it could suggest that the fraction of another site is increasing. Here, the error bars for f_{sum} were omitted, as they would be identical to those shown for f_{BC}.

The qualitative behaviour of both graphs is very similar, with only minor differences. Firstly, both fractions increase between 30°C and 300°C, although the increase in f_{BC} is more pronounced. Between 300°C and 600°C, the bond-centre fraction f_{BC} continues to increase in sample #530, but less steeply than before, while in sample #565 it starts to decrease slightly. The substitutional fraction f_S keeps increasing, though very slowly, showing an approximately linear trend. Finally, between 600°C and 900°C, f_{BC} decreases sharply in sample #530, which also causes the sum fraction f_{sum} to decrease; this could indicate that at higher temperatures, some other type of site might be forming, although we could not identify which one. In sample #565, f_{BC} also decreases, but less abruptly, and f_S continues its gradual increase following the same tendency.

These minor qualitative differences between the two samples could be due to the accuracy of the sample temperature read-out, which is estimated around $\pm$10º: in sample #530, the actual temperature could have been slightly below 600°C, while in sample #565, it could have been slightly above 600°C. We do not know the precise behaviour of the site fractions in the vicinity of that temperature.

One notable quantitative difference between the two samples is the overall value of the site fractions: in sample #565, the fractions are approximately half of those observed in sample #530. There are several possible explanations for this. As mentioned earlier, the background corrections might not have been perfect, but we do not believe this alone could account for such a large difference. Another possibility could be the difference in the implantation fluence; however, simulations of the resulting lattice damage suggest that this difference is not sufficient to explain a halving of the site fractions. A further possibility is that, during the implantation of sample #565, the beam might have partially missed the sample, with some portion of the beamspot hitting the sample holder instead. This would reduce the effective activity of the implanted isotope.

The most plausible explanation is that the simulations introduced a systematic error due to differences in the beam energy, which drastically reduced the site-fraction intensities in sample #565.

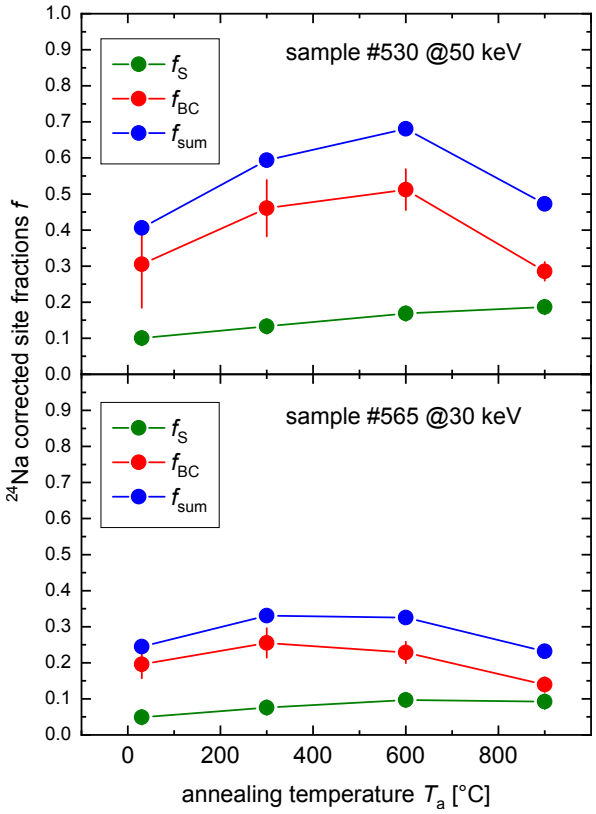

Figure 3.3: Site fractions f versus annealing temperature T_a for two different samples with different beam implantation intensities. The quantities, f_S, f_{BC}, and f_{sum} represent the fractions at the substitutional site, the bond-centre site, and the sum of these two fractions, respectively.

These results are similar to those previously obtained for magnesium (Mg). In that study, the largest fitted fractions corresponded to BC sites (42% at RT; 30% at 800 °C), while smaller fractions were associated with S sites (15% at RT; 14% at 800 °C). These findings are consistent with our results, showing that the BC configuration predominates over S sites, and that the BC fraction decreases at higher temperatures (800 °C). That can be explained due to their similar electron configurations, Mg and Na would be expected to adopt similar configurations in the diamond lattice due to their comparable chemical properties. It remains possible that some additional site could appear at high annealing temperatures,

which has not yet been identified in this study. A comprehensive description of the Mg study can be found in [24].

In terms of theoretical predictions, the substitutional Na and the NaV full-vacancy configurations are associated with the substitutional site, while the NaV split-vacancy configuration corresponds to the bond-centre site. Since the NaV full-vacancy configuration is theoretically predicted to be unstable, we assume that the observed substitutional fraction represents only the true substitutional Na, without a nearby vacancy. These configurations are theoretically predicted to be optically active, exhibiting both a zero-phonon line (ZPL) and a phonon sideband (PSB), with specific values discussed in subsection 1.1.10. A search for these features was the focus of our PL studies, described in the following.

3.2. Photoluminescence

In this work, we measured four different diamond samples implanted with the stable isotope ^{23}Na at an energy of 50 keV. For each sample, the right half of the diamond surface was first covered, while the left side was implanted with 4.5×10^{12} atoms/cm^2. The cover was then removed, and the entire sample was implanted with 5×10^{11} atoms/cm^2, resulting in a total fluence of 5×10^{12} atoms/cm^2 on the left side and 5×10^{11} atoms/cm^2 on the right side. This allowed us to compare the results for a tenfold difference in fluence. We used two EL diamond samples, one of which was annealed at 900°C, and two SC diamond samples, again with one of them annealed at 900°C. The other two samples were kept unannealed. The samples were laser-marked to ensure there was no ambiguity about the front and back sides, as well as to clearly distinguish between the high- and low-fluence implanted sides.

These samples were not implanted with ^{24}Na, the radioactive isotope typically used in emission channeling experiments. By the time we had to perform the PL experiments for this thesis, the PL laboratory at ISOLDE had not yet been approved for use with radioactive samples. Consequently, we could not perform radioactive photoluminescence as initially proposed. To still include photoluminescence research in this thesis, we prepared these four samples at KU Leuven and brought them to ISOLDE to measure the photoluminescence lines of the stable sodium implantation. Because of this, we could not correlate the decay of radioactive sodium with a decrease in the PL signal. This is why, in these subsections of the thesis, we present simple PL, rather than its radioactive variety.

Before discussing the acquired data, I will briefly summarise the samples studied, as shown in Table 3.1. Firstly, we measured the two samples which were annealed at 900°C; afterwards, we measured the unannealed samples, which are listed in the table with an annealing temperature of 30°C.

Label	Type	T_a
E012	EL	900°C
L010	SC	900°C
E013	EL	30°C
L011	SC	30°C

Table 3.1: Overview of samples used in the PL experiment.

We started with the annealed samples because it is expected that ion-implanted colour centres in diamond only become optically active after annealing. During implantation, significant damage is introduced into the lattice, and the implanted atoms may initially not be located in their stable positions. Therefore, it was expected that if any of the samples were to show a sodium-related emission line, it would be these annealed ones. Between the two annealed samples, we first measured the EL sample, since its lower concentration of nitrogen and other impurities should result in fewer unwanted lines in the spectrum.

For all samples, we began by searching for the sodium peaks, scanning around the wavelength regions predicted theoretically, i.e. around 500 nm and 800 nm. After identifying a suspected peak, we performed a Z-scan (depth profiling) to determine whether the signal originated from a surface or bulk defect. As the sodium was implanted, we expected the defect to be near the surface, which would appear as a peak-like response, which reflects the depth resolution of the ”confocal” PL set-up. Once the presence of a candidate peak was confirmed, we performed an XY-scan across the entire sample to determine whether the signal followed the implanted pattern. These two measurements also enabled us to perform background correction, as will be shown later. Finally, we acquired the full emission spectrum in the wavelength range 475 nm to $\sim$800 nm from both the high-fluence side (left side) and the low-fluence side (right side).

In the discussion of the results, we will first analyse the full spectrum acquired to identify and discuss the peaks observed. Next, we will present the Z-scan to confirm the nature of the signal, followed by the XY-scan, and, if necessary, additional data.

The analysis of the sample's lower fluence region will not be addressed here, as the signals resemble those observed at higher fluence but are weaker and noisier, if detectable at all. Therefore, we will focus solely on the results from the higher fluence region. In the results section, the data are presented in the same sequence in which they were measured.

3.2.1 Analysis of E012 Sample

We started acquiring spectra of E012 (which was annealed at 900°C) at a few points and observed a peak at 503 nm in different locations (spots) on the sample, as we can see in Figures 3.4 and 3.5. This value is close to the theoretical value of 487 nm expected for the NaV centre [21]. However, in the wavelength range expected for the Na_s centre around 779/832 nm [21], we did not observe any peak. On the left side of the sample, the 503 nm peak was stronger than on the right side, as expected from the implantation pattern. We adjusted the polariser to 90º in order to minimise the first-order Raman contribution.

To acquire the full spectrum, we collected data at five different central wavelengths, manually changing the measurement location (spot) each time rather than using the automatic range function, as shown in the legend of Fig.3.4. All other acquisition parameters were kept constant across the different central wavelengths: an aperture width (APT) of 60 μm, an exposure time (ET) of 10 s, and 30 averages (AVG). We used the blue laser at a power of 5 mW.

As the resulting curves exhibited considerable noise, we applied a **Savitzky–Golay filter** [1] from the SciPy library to smooth the data, preserving the main features without significantly altering the underlying signal [59].

In the resulting full spectrum, we observe that only in the blue curve (with CW = 530 nm) does a peak appear; in the other curves, no significant signal is detected. The inclination visible in the curves is caused by a misalignment inside the spectrometer. This systematic effect appears consistently across all curves and is therefore not related to the response of the sample itself.

[1] The Savitzky–Golay filter smooths noisy data by fitting successive subsets of adjacent points with low-degree polynomials, preserving important features like peak height and width better than simple averaging filters.

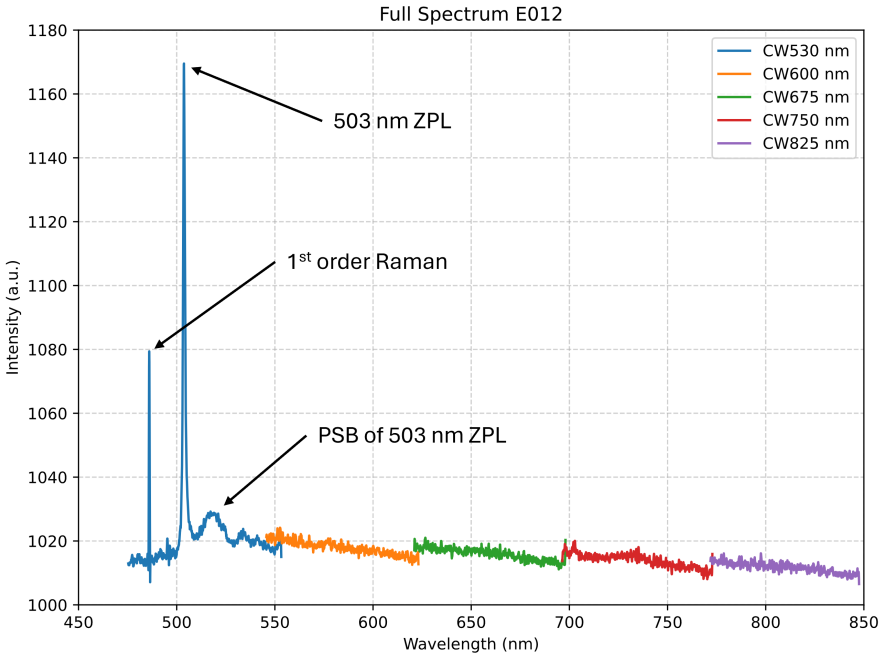

Figure 3.4: Full spectrum of the E012 sample.

Knowing the wavelength of our blue laser (457 nm), we can use Eq.1.4 to calculate the positions of the first- and second-order Raman peaks, which should appear at approximately 486 nm and 515 nm, respectively.

Focusing on the blue curve in Fig.3.5, we can clearly see the first-order Raman peak around 486 nm. However, the second-order Raman peak near 515 nm overlaps with the phonon sideband of the 503 nm peak, which extends from approximately 510 nm to 530 nm, resulting in a PSB with a width of about 20 nm.

Raman lines are typically very narrow, with their width often limited by the resolution of the spectrometer, which itself depends on the chosen aperture width (APT). In contrast, for the APT values chosen in our measurements, the width of the ZPL is usually determined by the properties of the ensemble of defects that give rise to it.

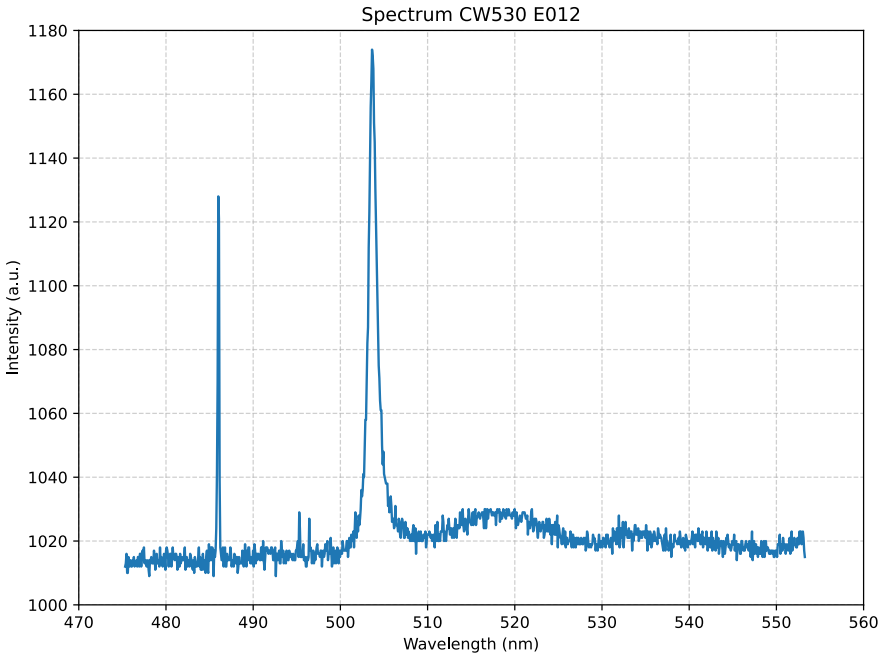

Figure 3.5: Spectrum of the E012 sample with a central wavelength of 530 nm.

Before continuing with the acquisition, we need to verify whether the 503 nm peak is a surface-related response, as expected due to the nature of the implantation process. In Fig.3.6, we used a power of 5 mW for the blue laser, and for the parameters: an APT of 60 μm, no averaging, and an ET of 5 s. This is not ideal, as the overall intensity of the spectrum will be low; however, as we will see later, another effect is occurring that compromises the quality of our Z-scans.

To calculate the intensity at each point, we selected a signal window centred at 505 nm with a width of $\pm$4 nm. For background correction, we chose a window centred at 545 nm, also with a width of $\pm$4 nm. As shown in Fig.3.5, this background region is flat and remains stable over time and under blue light exposure.

We can see a peak-like response of the signal, indicating that it is likely surface-related. Due to limited time, we opted only to verify the Z-scan quickly, so we did not use many points, which means we lack extensive statistics in this scan. We found the optimal z-value (the focus) to be 1.076 mm, as expected from the slope calculation for that spot.

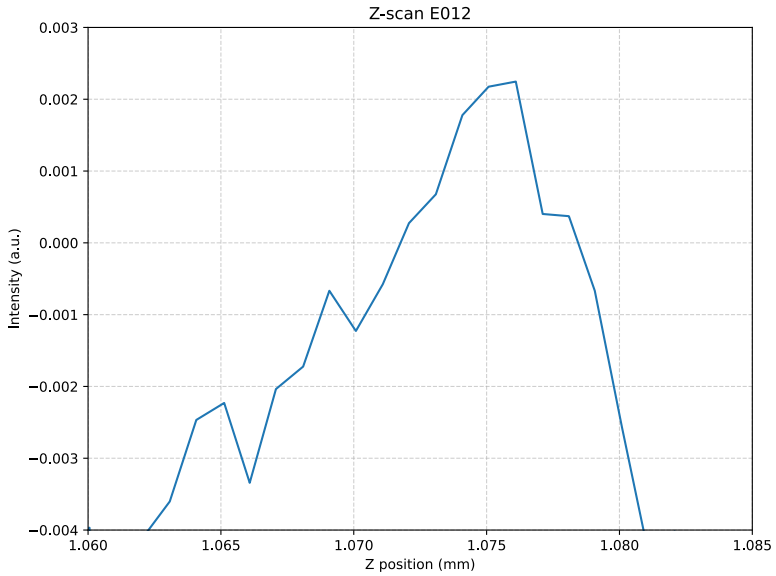

Figure 3.6: Z-scan of the E012 sample. Note that the fact that the intensity is turning negative is due to the chosen background subtraction.

For the XY-scan, we set the parameters as follows: CW of 530 nm, APT of 60 μm, ET of 10 s, and no AVG. We used the same windows as in the Z-scan to calculate the intensity at each point. For the scan configuration, we started from the bottom left corner of the sample and aimed to scan the entire area with sufficient resolution in about one hour. To achieve this, we chose a grid of 19×19 steps with a step size of 0.11 mm. Multiplying 19×0.11 gives 2.09 mm, which is slightly larger than the sample size of 2×2 mm^2, i.e. larger than the actual lateral dimension of the sample. So we expected to include a few points on the sample holder outside the diamond sample.

Looking at the XY-scan acquired for the E012 sample in Fig. 3.7, we can first observe that the implantation intensity pattern appears as expected: the high-fluence side shows an intensity approximately four times greater than the low-fluence side. The line separating both regions has high contrast, which is due to the relatively low resolution across that boundary; nevertheless, this indicates that, on a macroscale, the implantation separation was very well executed. In this plot, we can also see the specific spots where the detailed measurements were performed.

We decided to acquire measurements at different spots because we observed that, under prolonged blue laser exposure, the 503 nm peak decreased in intensity (quenched). After a sufficiently long time, the peak would become almost impossible to detect. This behaviour is illustrated in Fig.3.8.

At the border of the sample, particularly on the right-hand side, we can see points that do not follow the general trend and exhibit large variations; this is because those points were acquired on the sample holder rather than on the sample itself. At the bottom of the scan, the intensity is almost zero, so the 503 nm peak becomes comparable to the background.

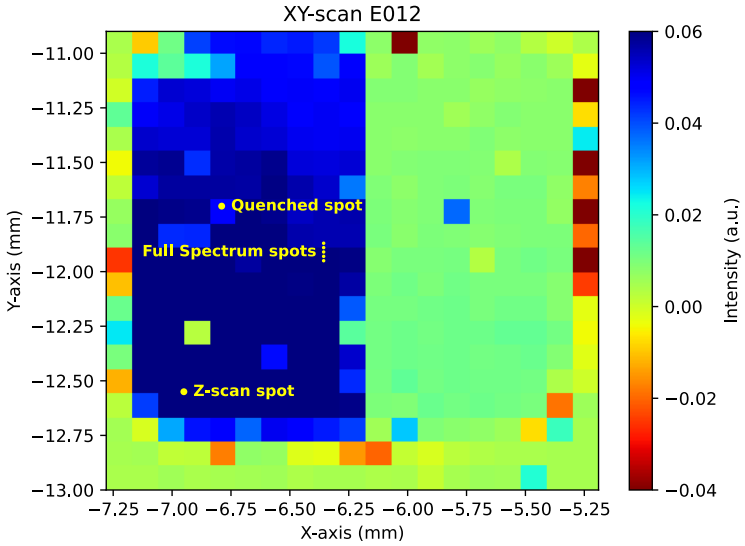

Figure 3.7: XY-scan of the entire E012 sample, with the measurement spots marked and labelled accordingly.

As mentioned earlier, Fig.3.8 shows the quenching effect observed in the 503 nm peak, using the same parameters as for the full spectrum. In Fig.3.8 (a), we present a time series measurement in which the peak intensity drops to almost half within just 40 seconds under a laser power of 10 mW. We also performed other time series measurements at laser powers of 2, 5, and 20 mW. In all cases, a decrease in peak intensity was observed, and the rate of this decrease correlated with the laser power used: the higher the power, the faster the quenching occurred.

We can also see a corresponding decrease in the phonon sideband (PSB), supporting that the PSB is indeed related to the adjacent peak. In Fig.3.8 (b), we show the signal from the sample after 20 minutes of blue laser exposure at 20 mW on the quenched spot; the peak has completely disappeared. A small ”bump” remains in that region, which is likely due to the second-order Raman, which is intrinsically weak. We also verified that even after one day, the peak did not recover at all.

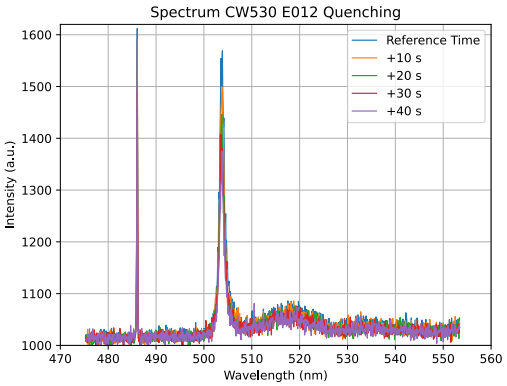

(a) Decrease of the 503 nm peak intensity over time under continuous blue laser exposure.

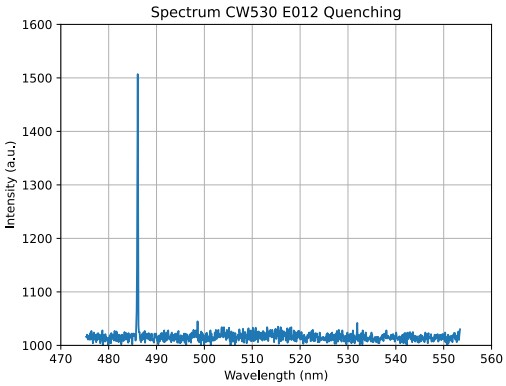

(b) 503 nm peak fully quenched after approximately 20 minutes.

Figure 3.8: Quenching effect on the 503 nm peak in sample E012.

We performed several Z-scans, but the results were not satisfactory due to on-spot quenching. This limited both the number of steps and the achievable signal intensity: rather than observing signal changes solely due to variations in the z-position, the measurements were dominated by quenching effects. As a result, many of the Z-scans showed inconsistent point-to-point variations, with increases due to improved focus but decreases caused by the quenching effect, unrelated to the actual focal position.

Consequently, we decided to perform an XY-scan, shown in Fig.3.9, on the quenched spot where the 503 nm peak and its PSB had completely disappeared. In this scan, we should see the outline of the laser beam spot as a region where the signal does not appear.

In this scan, we used a laser power of 5 mW and applied the same windows to calculate the intensity of each pixel as in the XY-scan of the whole sample. As the starting point, we chose a position offset by five steps diagonally to the bottom left of the quenched spot, with a grid of 11×11 steps, each of 2 μm. Measuring the major and minor axes of the elliptically shaped beam spot using the software *ImageJ*, and taking the edge of the last orange pixel as the boundary, we obtained diameters of 13 μm and 5 μm, respectively.

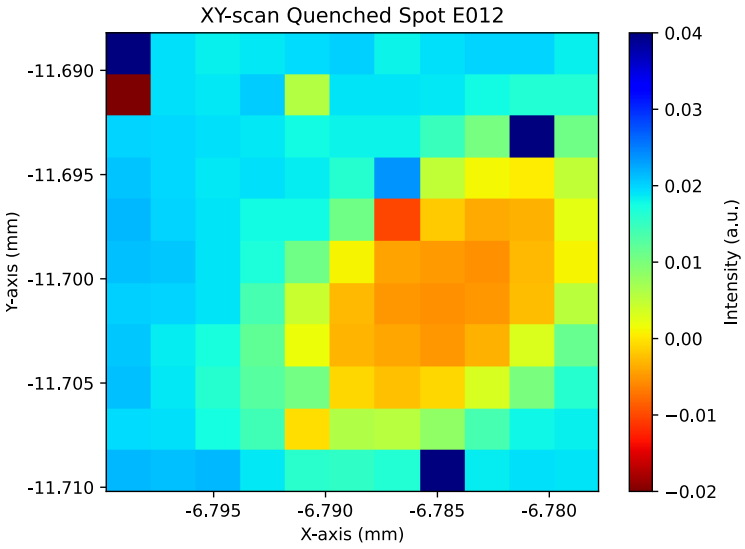

Figure 3.9: XY-scan in the quenched spot in E012.

As can be observed in Fig.3.9, the laser beam spot is visible but appears flattened and skewed along the diagonal, likely due to imperfect alignment of the set-up. Outside the beam spot, the 503 nm peak is still detectable, as these regions were not exposed to the blue laser previously to this fast XY-scan. At the exact centre of the beam spot, the 503 nm peak is most strongly quenched, corresponding to the area of highest laser intensity, which gradually diminishes moving away from the centre.

3.2.2 Analysis of L010 Sample

As with the E012 sample, we began by acquiring the full spectrum of L010 that was annealed at 900°C to identify the type of signal obtained and to check for the presence of any sodium-related peaks. The acquisition parameters were kept exactly the same as for the previous sample: an APT of 60 μm, an ET of 10 s, and 30 AVG. Since the overall luminescence intensity from SC-type samples was much higher than that from the highly pure EL-type samples, the laser power was adjusted to 2 mW to avoid excessive counts that could saturate the spectrometer.

From Fig.3.10, it can be observed that the overall behaviour of the signal differs significantly from that of the EL diamond sample, showing a broad band composed of two main ”bumps”, as well as other peaks. Due to the higher concentration of nitrogen, some nitrogen-related centres were formed, as indicated by the peak around 575 nm, which corresponds to the neutral nitrogen–vacancy centre (NV^0) [60]. The final peak in the red

curve (CW750) may correspond to the negatively charged silicon–vacancy centre (SiV^-) around 738 nm [60].

Regarding the small feature on the left, we believe it may be caused by the unpolished side of the sample (facing downwards), which could introduce back reflections and give rise to this signal. The upper side of the sample, where the sodium was implanted, is polished. The broad feature on the right corresponds to the NV^0 PSB at RT, as the centre has a low DW, i.e. a comparatively weak ZPL and a prominent PSB [60, 61].

Due to time constraints during the experiment, we did not acquire data for the part of the spectrum with CW825 nm. This region did not show any noticeable peaks or interesting features; the signal remained approximately constant at around 1000 a.u, i.e. the dark count response of the CCD.

In this sample, we observed a more intense 503 nm peak, which is unexpected. Under typical conditions, such peaks are usually more prominent in EL samples, as there are fewer competing centres. This suggests that the observed peak might originate from a different mechanism and may not be sodium-related. There is a possibility that the last peak observed corresponds to SiV^-.

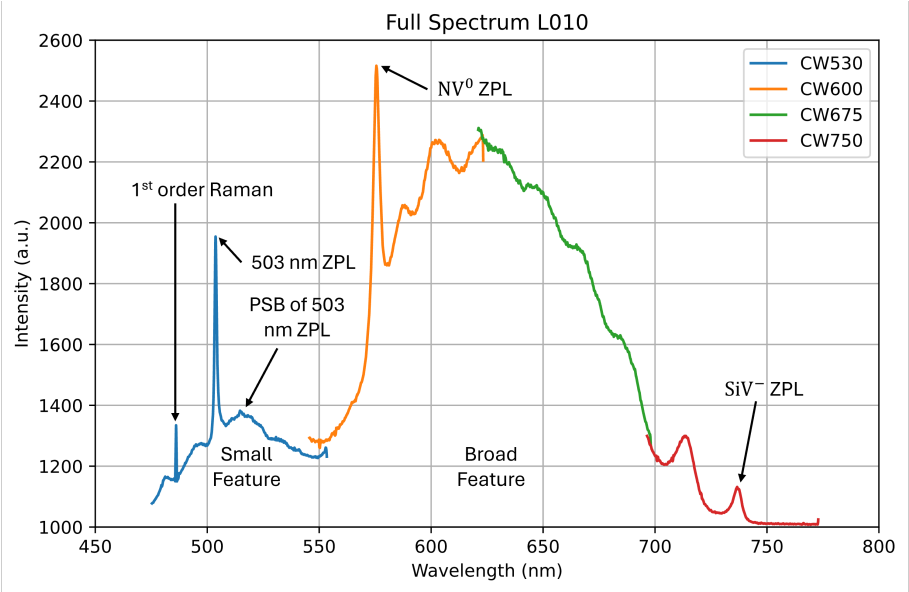

Figure 3.10: Full spectrum of the L010 sample.

For the Z-scan we acquired with an APT of 60 μm, no averaging, and an ET of 10 s, using the laser at 5 mW. To calculate the intensity at each point, we selected a signal window centred at 505 nm with a width of ± 4. For background correction, we chose a window centred at 490 nm, also with a width of ± 4. The background correction was more

challenging to define, as in the range of CW530 there is no perfectly flat region; the flattest section we identified was the part to the right of the 503 nm peak.

As illustrated in Fig.3.11, we observe a clear bulk-defect behaviour, appearing as a step-like profile rather than the peak-like response we initially expected. This suggests that the 503 nm peak could be due to something else and not necessarily related to sodium. Noting that the Z-position had to be shifted by approximately 250 µm to higher values compared to sample L013, since SC samples are only 0.25 mm thick, whereas EL samples are 0.5 mm thick.

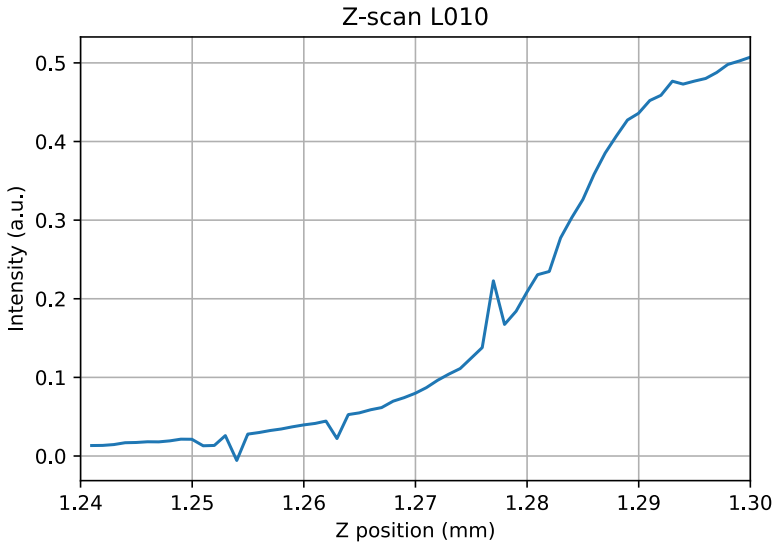

Figure 3.11: Z-scan of the L010 sample.

Anyway, we acquired the XY-scan to see if we get anything similar to the implantation pattern. We set the parameters as follows: CW of 530 nm, APT of 60 μm, ET of 10 s, and no AVG. We used the same windows as in the Z-scan to calculate the intensity at each point. For the scan configuration, we started from the bottom left corner of the sample and aimed to scan the entire area with sufficient resolution in about one hour. To achieve this, we chose a grid of 19×19 steps with a step size of 0.1620 mm. Multiplying 19×0.162 gives 3.078 mm, which is slightly larger than the sample size of 3×3 mm^2, i.e. larger than the actual lateral dimension of the sample. So we expected to include a few points on the sample holder outside the diamond sample once again.

As can be seen in Fig.3.12, we obtained a pattern similar to the implantation mask, although tilted by approximately 45º and varying along the diagonal, and it does not show as good a contrast as in the E012 sample. It seems that the distribution of the 503 nm

peak is not homogeneous, and it did not result from the implantation of ^{23}Na in the sample, or only partially so. We do not know precisely what the 503 nm peak corresponds to, but we can observe that its intensity was affected by the sodium implantation. We have also identified the spots where the full spectrum and the Z-scan were acquired. In this measurement, we also recorded a few points from the sample holder, which did not follow the local trend.

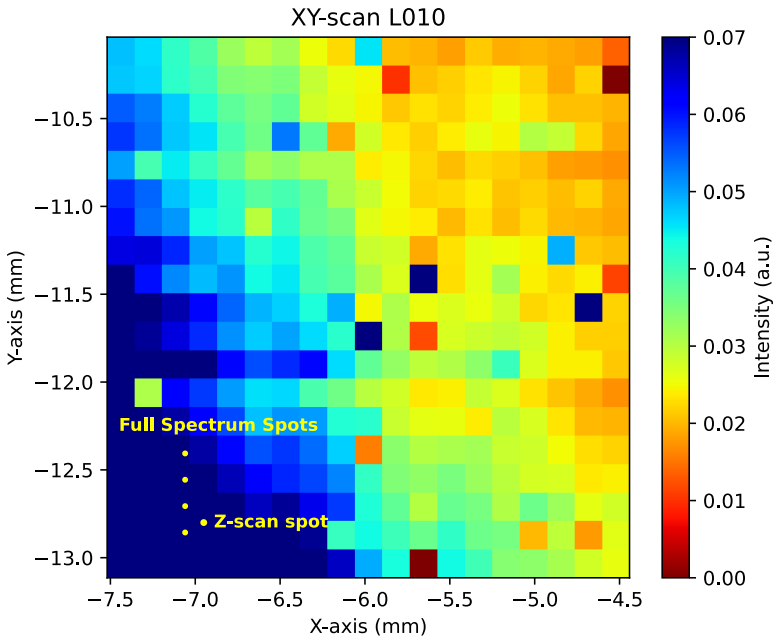

Figure 3.12: XY-scan of the entire L010 sample, with the measurement spots marked and labelled accordingly.

In Fig.3.13, we observe the same quenching behaviour of the 503 nm peak as previously seen in E012. In these measurements, we used a 5 mW blue laser for 18 minutes. The exposure time was not sufficient to completely quench the peak, as was done previously, due to time constraints. Once again, we also observe a decrease in the corresponding PSB.

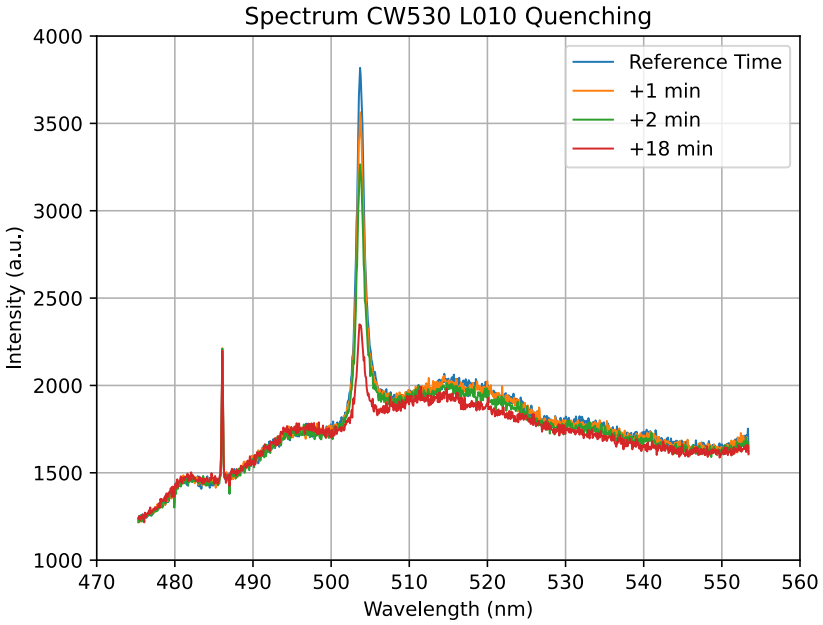

Figure 3.13: Quenching effect on the 503 nm peak in sample L010.

3.2.3 Analysis of Unannealed Samples (E013 and L011)

Due to the fact that these samples were not annealed, we do not expect to observe a sodium-related peak. As discussed previously, colour centres in the as-implanted state are usually optically inactive. For that reason, we will examine the data from both samples simultaneously.

To acquire the full spectra of both samples, we used an APT of 60 μm, an ET of 10 s, and 12 AVG, with a laser power of 5 mW and 2 mW for the E013 and L011 samples, respectively. The difference in laser power was to avoid saturating the spectrometer: in the SC sample (L011), the broadband produces much higher counts, which would saturate the detector at 5 mW. Instead of manually selecting central wavelengths, we used the range option, setting the range to [475,850] nm. We measured this range at the same spot on each sample to make better use of the available time; even if some peaks decrease under blue laser exposure, the averaging process allows us to still observe their average intensity. Both measurements were performed on the high-fluence side, but as we will see in the XY-scan, this choice is largely irrelevant because the samples were not annealed.

As depicted in Fig.3.14 (a), in the EL diamond sample, we observe the first-order Raman peak (around 486 nm), along with the second-order Raman feature appearing as a very weak broad peak centred near 515 nm. Comparing this to the annealed sample (E012)

shown in Fig.3.4, we see a similar trend above 550 nm, where there is essentially no measurable signal, and the spectra exhibit the same general slope. As expected, the 503 nm peak is completely absent in the unannealed sample.

In Fig.3.14 (b), we observe the same broadband feature due to the presence of NV^0, and the small feature which is attributed to the non-polished side of the sample. Compared to the annealed sample (Fig.3.10), the overall behaviour is very similar, although the last two peaks above 700 nm are much weaker; these peaks tend to increase upon annealing. We still detect the NV^0 peak around 575 nm. We measure a strong response from the neutral nitrogen vacancy (NV^0) while seeing no response from the negatively charged nitrogen vacancy (NV^-).

Unexpectedly, we also observe a peak at 503 nm. This peak appears in the sample with a higher nitrogen concentration and without annealing, suggesting that it is unlikely to be sodium-related.

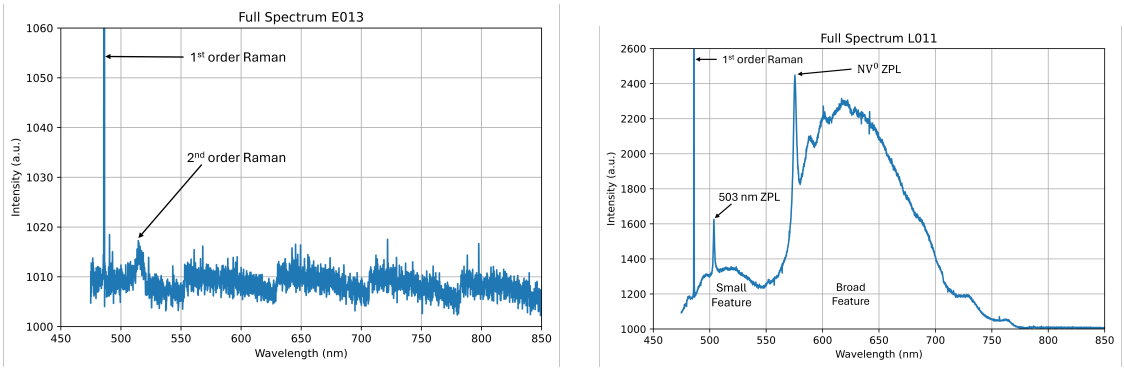

(a) E013. (b) L011.

Figure 3.14: Full Spectrum of the unannealed samples.

To confirm this, we measured a pristine SC diamond sample, shown in Fig.3.15, and obtained a spectrum similar to that in Fig.3.14 (b). The main difference is that the small feature is less pronounced in the pristine sample. The presence of the 503 nm peak in the pristine sample further supports the conclusion that this peak is not related to sodium. Initially, this feature was considered potentially sodium-associated because it appeared near the wavelength predicted by theoretical studies, and its intensity in the EL sample E012 annealed at 900°C was correlated with the implantation fluence.

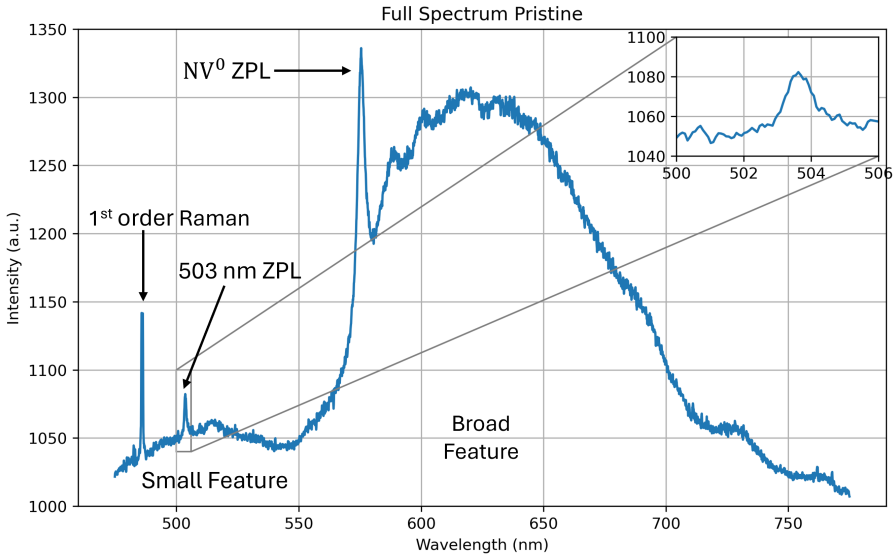

Figure 3.15: Full spectrum of the pristine SC diamond sample.

To acquire the XY-scans, we used the same parameters, the same integration windows to calculate the intensity at each pixel, and the same laser power as before, according to the diamond type. The two samples have different dimensions, as can be seen from the axes in Fig.3.16: in the EL diamond, the distance covered along the x- and y-axes is around 2 mm, whereas in the SC diamond it is approximately 3 mm, matching the physical size of each sample.

In Fig.3.16 (a), we observed almost no intensity of the 503 nm peak, as expected; we could not identify any trace of the sodium implantation, and the overall scale of intensities is very low. However, in Fig.3.16 (b), we see a noticeable difference between the high- and low-fluence sides of the implantation, although the top-left corner deviates from this general trend. Interestingly, on the side where the implantation fluence was higher, the intensity of the 503 nm peak was actually lower.

Since the sample was not annealed, and considering that the pristine SC diamond already exhibits the 503 nm peak, it is possible that Na implantation without annealing caused the optical deactivation of some 503 nm centres in the LO11 sample. This could explain why the 503 nm peak intensity appears higher in the regions of the sample that received the lower Na fluence. However, given the large spatial variations in the 503 nm peak intensity observed across all SC-grade samples, the observed XY-scan results may simply reflect the initial distribution of these centres.

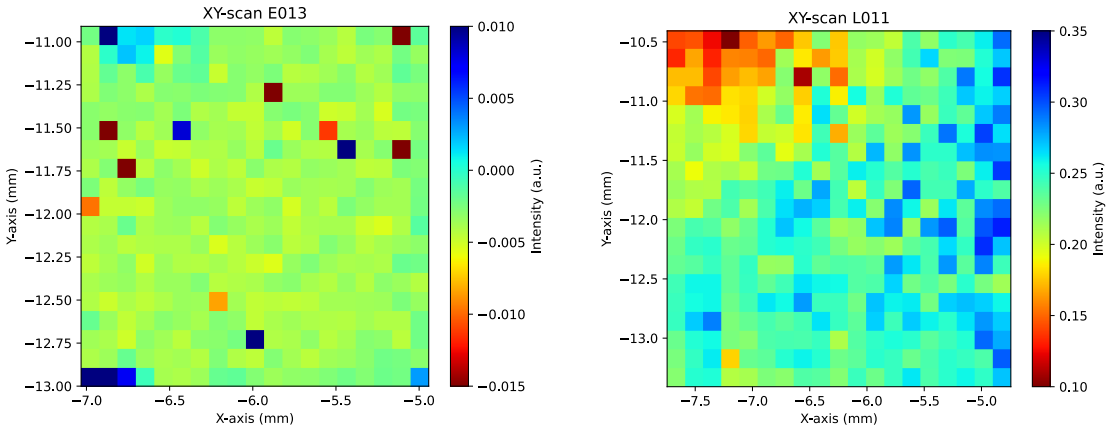

(a) E013. (b) L011.

Figure 3.16: XY-scan of the unannealed samples.

We can conclude that the SC diamond samples originating from Element Six (which are richer in nitrogen than the EL variety) exhibit the 503 nm peak, which could arise from nitrogen impurities incorporated during their fabrication. Thus, whereas in the SC samples the ZPL around 503 nm was readily visible in the unannealed diamonds, in the EL samples it was only observed after Na implantation followed by annealing at 900°C. This indicates that, in the EL-type samples, the introduction of radiation damage and subsequent annealing are required to induce its luminescence.

3.2.4 3H and H3 Centres

As previously discussed, the 503 nm peak is most likely not related to sodium. We identify two possible candidates for this peak: the H3 and 3H centres [60].

The **3H centre** in diamond is a radiation-induced defect, characterised by a sharp zero-phonon line at 503.5 nm. It typically forms in nitrogen-rich diamond after irradiation and annealing. However, its exact microscopic structure remains unclear. Although it is more prominently observed in nitrogen-containing diamond, this does not necessarily imply the direct involvement of nitrogen in its structure. Several models have been proposed, including an oxygen–vacancy pair [62], neutral interstitial hydrogen [63], and the single, isolated $\langle 100 \rangle$ split self-interstitial in diamond, most likely in a negative charge state [64, 65], the latter being the most commonly assumed nowadays. Its relative abundance in nitrogen-containing diamond could then be explained by its negative charge state, which is promoted by nitrogen acting as a donor.

The **H3 centre** in diamond is a nitrogen-related defect, characterised by a sharp zero-phonon line at 503.2 nm. It is generally accepted to consist of two next-nearest-neighbour substitutional nitrogen atoms separated by a vacancy, i.e. an N–V–N structure, presumably in a neutral charge state [62].

As shown in Fig.3.17, the spectra of the 3H and H3 centres can be compared. The RT photoluminescence spectrum of the 3H centre reported in [66] (Fig.3.17(a)) and also observed in [64] closely resembles the spectrum we measure for the 503 nm peak. It displays a sharp and well-defined ZPL followed by a PSB, a characteristic signature that strongly matches our experimental data. The 3H centre has a Debye–Waller factor of 0.3 at room temperature [66].

In contrast, the H3 centre exhibits a nearly absent ZPL at RT due to strong phonon coupling, corresponding to a DW of $\sim$0.015 [67], as shown in [60] (Fig.3.17(b)) and confirmed in [68]. Although the ZPL wavelengths of the two centres are very close, this strong difference in the relative intensities of the ZPL and phonon sideband (PSB) provides a reliable way to distinguish them.

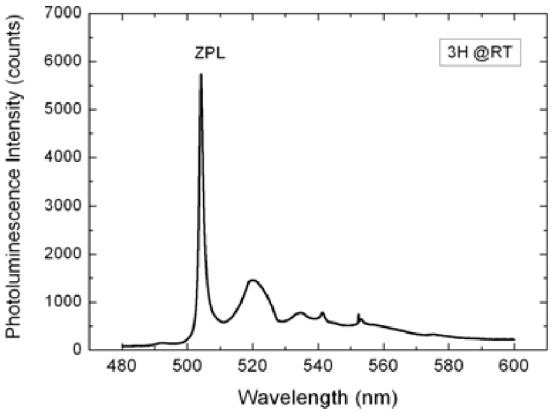

(a) Photoluminescence spectrum of the 3H centre at RT from [66].

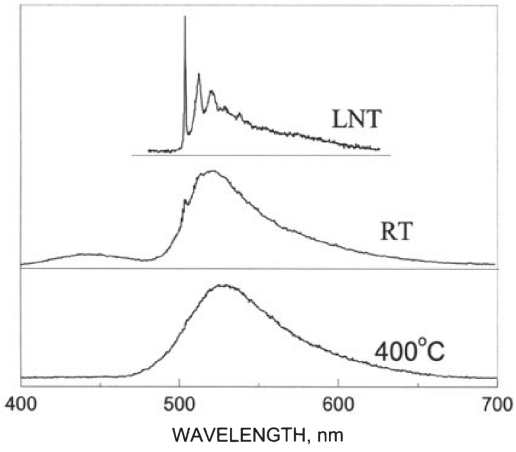

(b) Electroluminescence spectrum of the H3 centre at 77K (LNT), RT, and 400°C from [60].

Figure 3.17: Luminescence spectra of 3H and H3 centres.

Moreover, it has been reported that the 3H centre exhibits a reduction in intensity under prolonged laser exposure [63, 64], with a characteristic exponential decay that depends on the laser power and wavelength. In contrast, we did not find any evidence in the literature of quenching (bleaching) for the H3 centre.

Given the similarity in spectral shape between the 503 nm peak and the 3H centre, along

with the observed decrease in the 503 nm peak intensity under laser exposure, we are confident in concluding that this peak corresponds to the **3H centre**.

4. Conclusion

In this work, we investigated sodium as a colour centre in diamond, motivated by promising theoretical predictions highlighting its potential for quantum applications, and by the current lack of experimental studies on this centre. The experiments were carried out at ISOLDE/CERN, making use of the unique capability of this facility to provide radioactive species, in combination with the electron emission channeling (EC) and photoluminescence (PL) set-ups available on site.

We began by determining the most probable lattice sites that Na occupies in diamond using the EC set-up. Two single-crystal diamond samples (#530 and #565) were implanted at room temperature with radioactive ^{24}Na at different fluences (2.8×10^{13} and 5×10^{12} atoms/cm^2) and beam energies (50 keV and 30 keV), respectively. In both samples, we measured the anisotropy patterns around the $\langle100\rangle$, $\langle110\rangle$, $\langle111\rangle$, and $\langle211\rangle$ axes using a position-sensitive silicon pad detector, for three annealing temperatures: 300°C, 600°C, and 900°C, as well as for the as-implanted case (without annealing).

To identify the occupied sites, the experimental patterns were fitted (using the JavaFDD software) by simulated patterns calculated via the many-beam approach. The best fits corresponded to a mixture of substitutional (S) and bond-centre (BC) sites, consistent with theoretical predictions. Analysis of the site fractions as a function of annealing temperature revealed that at $T_a = 600$°C the BC site fraction reached a maximum of approximately 51%, corresponding to the NaV split-vacancy configuration. Above this temperature, the BC fraction decreased sharply, leading to a reduction in the combined fraction of S and BC sites. This behaviour suggests the possible formation of another, as yet unidentified, lattice configuration.

Having identified the most probable configurations and the corresponding wavelength range of interest, we further studied these systems using the PL set-up. Initially, we aimed to perform PL measurements on the radioactive counterpart (rPL); however, as CERN did not authorise the use of radioactive samples in the PL laboratory, we restricted our study to stable ^{23}Na. For this purpose, we implanted four different samples, each annealed at a distinct temperature, and for all samples we performed XY- and Z-scans, as well as acquired the full spectrum within our range of interest.

In the first measurements, carried out on sample E012 (annealed), we observed a peak at approximately 503 nm, close to the theoretically predicted wavelength of 487 nm. The zero-phonon line (ZPL) was sharp, with a small phonon sideband (PSB), indicating a high Debye-Waller factor, but no other significant spectral features were detected. Using this peak as a reference, we proceeded to characterise the sample with the scans. We found that the 503 nm peak was quenched after prolonged exposure to the blue laser.

When measurements were repeated on sample L010 (annealed), the behaviour differed, although the 503 nm peak was again observed and similarly quenched. Unexpectedly, when we measured unannealed samples (E013 and L011), where no 503 nm peak was anticipated, as colour centres typically require annealing to migrate to equilibrium positions and re-order their charge states to become optically active, we still detected the same peak. To confirm whether this feature was sodium-related, we measured a pristine SC diamond (with no implantation) and, once again, the 503 nm peak appeared.

A review of the literature on diamond colour centres revealed that this feature corresponds to the well-known 3H centre. Therefore, although no direct optical signal attributable to sodium was observed, we present the optical characterisation of single-crystal diamond samples fabricated by Element Six and implanted with stable sodium at various annealing temperatures.

In future work, it would be of interest to repeat the implantations and measurements in an attempt to detect any optical response from sodium centres. In particular, employing rPL can be especially promising. This would involve implanting ^{24}Na in the EC set-up, subsequently transferring those samples to the PL set-up, and exploiting the decay to observe a sodium-related optical signal potentially. In that respect, it would also be interesting to explore annealing temperatures higher than 900°C, which should be possible once the newly acquired electron beam annealing system becomes operational at ISOLDE. Moreover, the present work has established robust procedures and identified suitable parameters for rPL measurements, which are inherently time-sensitive and must therefore be conducted both rapidly and accurately. It is anticipated that later this year, rPL measurements with sodium will become feasible. Regarding the EC results, an additional avenue for investigation would be to search for the possible emergence of a third site and its characteristics.

References

[1] N. Savvides and T. J. Bell, "Hardness and elastic modulus of diamond and diamond-like carbon films," *Thin Solid Films*, vol. 228, no. 1-2, pp. 289–292, 1993. [Online]. Available: https://dx.doi.org/10.1016/0040-6090(93)90618-Y [Cited on page 1.]

[2] B. L. Green, A. T. Collins, and C. M. Breeding, "Diamond spectroscopy, defect centers, color, and treatments," *Reviews in Mineralogy and Geochemistry*, vol. 88, no. 1, pp. 637–688, 2022. [Online]. Available: https://dx.doi.org/10.2138/rmg.2022.88.12 [Cited on pages 1, 2, 3, 5, and 9.]

[3] S. J. Sque, "A first-principles study on bulk and transfer doping of diamond," *University of Exeter*, p. 239, 2007. [Cited on pages 1, 6, and 7.]

[4] E. Gaillou and G. R. Rossman, "Color in natural diamonds: The beauty of defects," *Rocks amp; Minerals*, vol. 89, no. 1, pp. 66–75, 2014. [Online]. Available: https://dx.doi.org/10.1080/00357529.2014.842839 [Cited on page 3.]

[5] U. Wahl, *Emission channeling: charged particle–solid interaction, detection and lattice location methods*, University of Lisbon, 2006. [Cited on pages 3, 14, 15, 16, 17, and 19.]

[6] M. N. R. Ashfold, J. P. Goss, B. L. Green, P. W. May, M. E. Newton, and C. V. Peaker, "Nitrogen in diamond," *Chemical Reviews*, vol. 120, no. 12, pp. 5745–5794, 2020. [Online]. Available: https://dx.doi.org/10.1021/acs.chemrev.9b00518 [Cited on pages 4 and 5.]

[7] A. Tallaire, J. Achard, F. Silva, O. Brinza, and A. Gicquel, "Growth of large size diamond single crystals by plasma assisted chemical vapour deposition: Recent achievements and remaining challenges," *Comptes Rendus. Physique*, vol. 14, no. 2-3, pp. 169–184, 2013. [Online]. Available: https://dx.doi.org/10.1016/j.crhy.2012.10.008 [Cited on page 4.]

[8] E. Six, "Diamond handbook," p. 32, 2024. [Cited on page 4.]

[9] E. S. D. B. GROUP, "Sc plate cvd 3.0x3.0mm, 0.25mm thick, <100>, pl." [Online]. Available: https://e6cvd.com/us/application/general/sc-plate-cvd-3-0x3-0x0-25mm-100-pl.html [Cited on page 4.]

[10] ——, "El sc plate 2.0x2.0mm, 0.50mm thick." [Online]. Available: https://e6cvd.com/us/application/all/el-sc-plate-2-0x2-0x0-5mm.html [Cited on page 4.]

[11] W. D. Callister and D. G. Rethwisch, *Materials science and engineering : an introduction*, 10th ed. Hoboken, NJ: Wiley, 2020. [Cited on page 4.]

[12] W. contributors, "Jablonski diagram." [Online]. Available: https://en.wikipedia.org/w/index.php?title=Jablonski_diagram&oldid=1292962118 [Cited on pages 5 and 6.]

[13] J. W. Verhoeven, "Glossary of terms used in photochemistry (iupac recommendations 1996)," *Pure and Applied Chemistry*, vol. 68, no. 12, pp. 2223–2286, 1996. [Online]. Available: https://dx.doi.org/10.1351/pac199668122223 [Cited on page 7.]

[14] C. Bradac, W. Gao, J. Forneris, M. E. Trusheim, and I. Aharonovich, "Quantum nanophotonics with group iv defects in diamond," *Nature Communications*, vol. 10, no. 1, 2019. [Online]. Available: https://dx.doi.org/10.1038/s41467-019-13332-w [Cited on page 8.]

[15] D. Riedel, I. Söllner, B. J. Shields, S. Starosielec, P. Appel, E. Neu, P. Maletinsky, and R. J. Warburton, "Deterministic enhancement of coherent photon generation from a nitrogen-vacancy center in ultrapure diamond," *Physical Review X*, vol. 7, no. 3, 2017. [Online]. Available: https://dx.doi.org/10.1103/physrevx.7.031040

[16] D. Chen, N. Zheludev, and W. Gao, "Building blocks for quantum network based on group iv split vacancy centers in diamond," *Advanced Quantum Technologies*, vol. 3, no. 2, p. 1900069, 2020. [Online]. Available: https://dx.doi.org/10.1002/qute.201900069 [Cited on page 8.]

[17] G. A. Waychunas, "Luminescence spectroscopy," *Reviews in Mineralogy and Geochemistry*, vol. 78, no. 1, pp. 175–217, 2014. [Online]. Available: https://dx.doi.org/10.2138/rmg.2014.78.5 [Cited on page 8.]

[18] K. Johnston, M. O. Henry, D. McCabe, E. McGlynn, M. Dietrich, E. Alves, and M. Xia, "Identification of donor-related impurities in zno using photoluminescence and radiotracer techniques," *Physical Review B*, vol. 73, no. 16, 2006. [Online]. Available: https://dx.doi.org/10.1103/physrevb.73.165212 [Cited on page 8.]

[19] L. Pereira, U. Wahl, J. Correia, Guilherme, A. Costa, E. David Bosne, and Lima, "Quantum colour centers in diamond studied by emission channeling with short-lived

isotopes (ec-sli) and radiotracer photoluminescence," 2020. [Online]. Available: https://cds.cern.ch/record/2717973

[20] L. Pereira, U. Wahl, J. Correia, B. Biesmans, A. Costa, M. da Silva, E. David Bosne, and Lamelas, "Quantum colour centers in diamond studied by emission channeling with short-lived isotopes (ec-sli) and radiotracer photoluminescence," 2023. [Online]. Available: https://cds.cern.ch/record/2845693 [Cited on page 8.]

[21] J. Davidsson, W. Stenlund, A. S. Parackal, R. Armiento, and I. A. Abrikosov, "Na in diamond: high spin defects revealed by the adaq high-throughput computational database," *npj Computational Materials*, vol. 10, no. 1, 2024. [Online]. Available: https://dx.doi.org/10.1038/s41524-024-01292-9 [Cited on pages 10, 11, 12, and 43.]

[22] *What is Density Functional Theory?*, 2009, pp. 1–33, wiley Online Books. [Online]. Available: https://doi.org/10.1002/9780470447710.ch1 [Cited on page 10.]

[23] E. B. Lombardi, A. Mainwood, and K. Osuch, "Ab initiostudy of lithium and sodium in diamond," *Physical Review B*, vol. 76, no. 15, 2007. [Online]. Available: https://dx.doi.org/10.1103/PhysRevB.76.155203 [Cited on page 10.]

[24] E. Corte, G. Andrini, E. Nieto Hernández, V. Pugliese, A. Costa, L. M. C. Pereira, A. Vantomme, J. G. Correia, P. Olivero, U. Wahl, and J. Forneris, "Magnesium-vacancy optical centers in diamond," *ACS Photonics*, vol. 10, no. 1, pp. 101–110, 2023. [Online]. Available: https://dx.doi.org/10.1021/acsphotonics.2c01130 [Cited on pages 11 and 41.]

[25] M. W. Doherty, N. B. Manson, P. Delaney, F. Jelezko, J. Wrachtrup, and L. C. L. Hollenberg, "The nitrogen-vacancy colour centre in diamond," *Physics Reports*, vol. 528, no. 1, pp. 1–45, 2013. [Online]. Available: https://dx.doi.org/10.1016/j.physrep.2013.02.001 [Cited on page 12.]

[26] L. V. H. Rodgers, L. B. Hughes, M. Xie, P. C. Maurer, S. Kolkowitz, A. C. Bleszynski Jayich, and N. P. De Leon, "Materials challenges for quantum technologies based on color centers in diamond," *MRS Bulletin*, vol. 46, no. 7, pp. 623–633, 2021. [Online]. Available: https://dx.doi.org/10.1557/s43577-021-00137-w [Cited on page 13.]

[27] J. Cai, F. Jelezko, and M. B. Plenio, "Hybrid sensors based on colour centres in diamond and piezoactive layers," *Nature Communications*, vol. 5, no. 1, 2014. [Online]. Available: https://dx.doi.org/10.1038/ncomms5065 [Cited on page 13.]

[28] I. Aharonovich, A. D. Greentree, and S. Prawer, "Diamond photonics," *Nature Photonics*, vol. 5, no. 7, pp. 397–405, 2011. [Online]. Available: https://dx.doi.org/10.1038/nphoton.2011.54 [Cited on page 13.]

[29] L. Childress and R. Hanson, "Diamond nv centers for quantum computing and quantum networks," *MRS Bulletin*, vol. 38, no. 2, pp. 134–138, 2013. [Online]. Available: https://dx.doi.org/10.1557/mrs.2013.20 [Cited on page 13.]

[30] S. Ditalia Tchernij, T. Lühmann, T. Herzig, J. Küpper, A. Damin, S. Santonocito, M. Signorile, P. Traina, E. Moreva, F. Celegato, S. Pezzagna, I. P. Degiovanni, P. Olivero, M. Jakšić, J. Meijer, P. M. Genovese, and J. Forneris, "Single-photon emitters in lead-implanted single-crystal diamond," *ACS Photonics*, vol. 5, no. 12, pp. 4864–4871, 2018. [Online]. Available: https://dx.doi.org/10.1021/acsphotonics.8b01013 [Cited on page 14.]

[31] S. D. Tchernij, T. Herzig, J. Forneris, J. Küpper, S. Pezzagna, P. Traina, E. Moreva, I. P. Degiovanni, G. Brida, N. Skukan, M. Genovese, M. Jakšić, J. Meijer, and P. Olivero, "Single-photon-emitting optical centers in diamond fabricated upon sn implantation," *ACS Photonics*, vol. 4, no. 10, pp. 2580–2586, 2017. [Online]. Available: https://dx.doi.org/10.1021/acsphotonics.7b00904

[32] E. Neu, D. Steinmetz, J. Riedrich-Möller, S. Gsell, M. Fischer, M. Schreck, and C. Becher, "Single photon emission from silicon-vacancy colour centres in chemical vapour deposition nano-diamonds on iridium," *New Journal of Physics*, vol. 13, no. 2, p. 025012, 2011. [Online]. Available: https://dx.doi.org/10.1088/1367-2630/13/2/025012 [Cited on page 14.]

[33] H. Hofsäss and G. Lindner, "Emission channeling and blocking," *Physics Reports*, vol. 201, no. 3, pp. 121–183, 1991. [Online]. Available: https://dx.doi.org/10.1016/0370-1573(91)90121-2 [Cited on page 14.]

[34] U. Wahl, J. G. Correia, A. Costa, E. David-Bosne, L. M. C. Pereira, L. M. Amorim, V. Augustyns, K. Temst, A. Vantomme, M. R. Da Silva, D. J. Silva, J. P. Araújo, P. Miranda, and K. Bharuth-Ram, "Emission channeling with short-lived isotopes (ec-sli) at cern's isolde facility." WORLD SCIENTIFIC, 2015, Conference Proceedings, pp. 563–573. [Online]. Available: https://dx.doi.org/10.1142/9789814632041_0061

[35] H. Hofsäss, "Emission channeling," *Hyperfine Interactions*, vol. 97-98, no. 1, pp. 247–283, 1996. [Online]. Available: https://dx.doi.org/10.1007/bf02150180

[36] U. Wahl, "Emission channeling studies of li in semiconductors," *Physics Reports*, vol. 280, no. 3-4, pp. 145–285, 1997. [Online]. Available: https://dx.doi.org/10.1016/S0370-1573(96)00021-X [Cited on page 14.]

[37] K. S. Krane and D. Halliday, *Introductory nuclear physics*. New York: Wiley, 1988. [Cited on page 14.]

[38] W. Leo, *Techniques for Nuclear and Particle Physics Experiments: A How-to Approach*. Springer Berlin Heidelberg, 2012. [Online]. Available: https://books.google.pt/books?id=yc4qBAAAQBAJ [Cited on page 15.]

[39] G. Schatz and A. Weidinger, *Nuclear condensed matter physics. Nuclear methods and applications*. United Kingdom: Wiley, 1996. [Cited on pages 15, 16, and 17.]

[40] J. U. Andersen, *Channeling and Blocking of Energetic Particles in Crystals*. Springer International Publishing, 2014, pp. 549–588. [Online]. Available: https://dx.doi.org/10.1007/978-3-319-05564-0_11 [Cited on pages 15, 16, and 17.]

[41] J. Lindhard, "Influence of crystal lattice on motion of energetic charged particles," 1965. [Online]. Available: https://www.osti.gov/biblio/4546261 [Cited on page 17.]

[42] K. Johnston, J. Schell, J. G. Correia, M. Deicher, H. P. Gunnlaugsson, A. S. Fenta, E. David-Bosne, A. R. G. Costa, and D. C. Lupascu, "The solid state physics programme at isolde: recent developments and perspectives," *Journal of Physics G: Nuclear and Particle Physics*, vol. 44, no. 10, p. 104001, 2017. [Online]. Available: https://dx.doi.org/10.1088/1361-6471/aa81ac [Cited on page 18.]

[43] U. Wahl, "Advances in electron emission channeling measurements in semiconductors," *Hyperfine Interactions*, vol. 129, no. 1-4, pp. 349–370, 2000. [Online]. Available: https://dx.doi.org/10.1023/a:1012697429920 [Cited on page 18.]

[44] E. David-Bosne, U. Wahl, J. G. Correia, T. A. L. Lima, A. Vantomme, and L. M. C. Pereira, "A generalized fitting tool for analysis of two-dimensional channeling patterns," *Nuclear Instruments and Methods in Physics Research Section B: Beam Interactions with Materials and Atoms*, vol. 462, pp. 102–113, 2020. [Online]. Available: https://dx.doi.org/10.1016/j.nimb.2019.10.029 [Cited on pages 19 and 34.]

[45] E. D. Bosne, “Emission channeling lattice location studies in semiconductors using highly pixellated timepix detectors,” *Instituto Superior Técnico*, 2020. [Cited on page 20.]

[46] N. E. A. (NEA), “Janis database,” 2025. [Online]. Available: https://www.oecd-nea.org/jcms/pl_39910/janis [Cited on page 20.]

[47] O. Brüning, M. Klein, S. Myers, and L. Rossi, “70 years at the high-energy frontier with the cern accelerator complex,” *Nature Reviews Physics*, vol. 6, no. 10, pp. 628–637, 2024. [Online]. Available: https://dx.doi.org/10.1038/s42254-024-00758-5 [Cited on pages 21 and 22.]

[48] G. Aad, T. Abajyan, B. Abbott, J. Abdallah, and S. Abdel Khalek, “Observation of a new particle in the search for the standard model higgs boson with the atlas detector at the lhc,” *Physics Letters B*, vol. 716, no. 1, pp. 1–29, 2012. [Online]. Available: https://dx.doi.org/10.1016/j.physletb.2012.08.020 [Cited on page 21.]

[49] T. Berners Lee, R. Cailliau, J. F. Groff, and B. Pollermann, “World wide web: The information universe,” *Internet Research*, vol. 2, no. 1, pp. 52–58, 1992. [Online]. Available: https://doi.org/10.1108/eb047254 [Cited on page 21.]

[50] CERN, “The cern accelerator complex,” 2022. [Online]. Available: https://cds.cern.ch/record/2800984 [Cited on page 22.]

[51] V. Barozier, “Vincent barozier and the isolde technical team,” 2025. [Cited on page 23.]

[52] R. Catherall, W. Andreazza, M. Breitenfeldt, A. Dorsival, G. J. Focker, T. P. Gharsa, G. T J, J. L. Grenard, F. Locci, P. Martins, S. Marzari, J. Schipper, A. Shornikov, and T. Stora, “The isolde facility,” *Journal of Physics G: Nuclear and Particle Physics*, vol. 44, no. 9, p. 094002, 2017. [Online]. Available: https://dx.doi.org/10.1088/1361-6471/aa7eba [Cited on pages 23 and 24.]

[53] U. Köster, “Isolde target and ion source chemistry,” *Radiochimica Acta*, vol. 89, no. 11-12, pp. 749–756, 2001. [Online]. Available: https://dx.doi.org/10.1524/ract.2001.89.11-12.749 [Cited on pages 23 and 24.]

[54] V. I. Mishin, V. N. Fedoseyev, H. J. Kluge, V. S. Letokhov, H. L. Ravn, F. Scheerer, Y. Shirakabe, S. Sundell, and O. Tengblad, “Chemically selective laser ion-source for the cern-isolde on-line mass separator facility,” *Nuclear*

Instruments and Methods in Physics Research Section B: Beam Interactions with Materials and Atoms, vol. 73, no. 4, pp. 550–560, 1993. [Online]. Available: https://dx.doi.org/10.1016/0168-583x(93)95839-w [Cited on page 24.]

[55] M. R. Silva, U. Wahl, J. G. Correia, L. M. Amorim, and L. M. C. Pereira, "A versatile apparatus for on-line emission channeling experiments," *Review of Scientific Instruments*, vol. 84, no. 7, p. 073506, 2013. [Online]. Available: https://dx.doi.org/10.1063/1.4813266 [Cited on page 26.]

[56] J. F. Ziegler, M. D. Ziegler, and J. P. Biersack, "Srim – the stopping and range of ions in matter (2010)," *Nuclear Instruments and Methods in Physics Research Section B: Beam Interactions with Materials and Atoms*, vol. 268, no. 11-12, pp. 1818–1823, 2010. [Online]. Available: https://dx.doi.org/10.1016/j.nimb.2010.02.091 [Cited on page 33.]

[57] P. R. Bevington and D. K. Robinson, *Data reduction and error analysis for the physical sciences*. McGraw-Hill, 2003. [Cited on page 34.]

[58] J. Beyer, T. B. E. Grønbech, J. Zhang, K. Kato, and B. Brummerstedt Iversen, "Electron density and thermal motion of diamond at elevated temperatures," *Acta Crystallographica Section A Foundations and Advances*, vol. 79, no. 1, pp. 41–50, 2023. [Online]. Available: https://dx.doi.org/10.1107/s2053273322010154 [Cited on page 34.]

[59] T. Konstantinovsky, "Introduction to the savitzky–golay filter: A comprehensive guide (using python)," 2024. [Online]. Available: https://medium.com/pythoneers/introduction-to-the-savitzky-golay-filter-a-comprehensive-guide-using-python-b2dd07a8e2ce [Cited on page 43.]

[60] A. M. Zaitsev, "Optical properties of diamond," 2001. [Online]. Available: https://dx.doi.org/10.1007/978-3-662-04548-0 [Cited on pages 49, 50, 56, and 57.]

[61] Y.-F. Gao, J.-M. Lai, Y.-J. Sun, X.-L. Liu, C.-N. Lin, P.-H. Tan, C.-X. Shan, and J. Zhang, "Charge state manipulation of nv centers in diamond under phonon-assisted anti-stokes excitation of nv0," *ACS Photonics*, vol. 9, no. 5, pp. 1605–1613, 2022. [Online]. Available: https://dx.doi.org/10.1021/acsphotonics.1c01928 [Cited on page 50.]

[62] J. Walker, "Optical absorption and luminescence in diamond," *Reports on Progress in Physics*, vol. 42, no. 10, pp. 1605–1659, 1979. [Online]. Available: https://dx.doi.org/10.1088/0034-4885/42/10/001 [Cited on pages 56 and 57.]

[63] I. I. Vlasov, V. G. Ralchenko, and E. Goovaerts, "Laser-induced transformation of 3h defects in diamond," *physica status solidi (a)*, vol. 193, no. 3, pp. 489–493, 2002. [Online]. Available: https://dx.doi.org/10.1002/1521-396X(200210)193:3<489::AID-PSSA489>3.0.CO;2-M [Cited on pages 56 and 57.]

[64] J. W. Steeds, T. J. Davis, S. J. Charles, J. M. Hayes, and J. E. Butler, "3h luminescence in electron-irradiated diamond samples and its relationship to self-interstitials," *Diamond and Related Materials*, vol. 8, no. 10, pp. 1847–1852, 1999. [Online]. Available: https://dx.doi.org/10.1016/S0925-9635(99)00144-2 [Cited on pages 56 and 57.]

[65] J. W. Steeds and S. Kohn, "Annealing of electron radiation damage in a wide range of ib and iia diamond samples," *Diamond and Related Materials*, vol. 50, pp. 110–122, 2014. [Online]. Available: https://dx.doi.org/10.1016/j.diamond.2014.09.012 [Cited on page 56.]

[66] S. Pezzagna, D. Rogalla, D. Wildanger, J. Meijer, and A. Zaitsev, "Creation and nature of optical centres in diamond for single-photon emission—overview and critical remarks," *New Journal of Physics*, vol. 13, no. 3, p. 035024, 2011. [Online]. Available: https://dx.doi.org/10.1088/1367-2630/13/3/035024 [Cited on page 57.]

[67] G. Davies, "Vibronic spectra in diamond," *Journal of Physics C: Solid State Physics*, vol. 7, no. 20, pp. 3797–3809, 1974. [Online]. Available: https://dx.doi.org/10.1088/0022-3719/7/20/019 [Cited on page 57.]

[68] A. Pant, C. Gupta, and K. Senkalla, "Reduced photothermal heating in diamonds enriched with h3 point defects," *Journal of Applied Physics*, vol. 131, no. 23, p. 234401, 2022. [Online]. Available: https://dx.doi.org/10.1063/5.0090661 [Cited on page 57.]